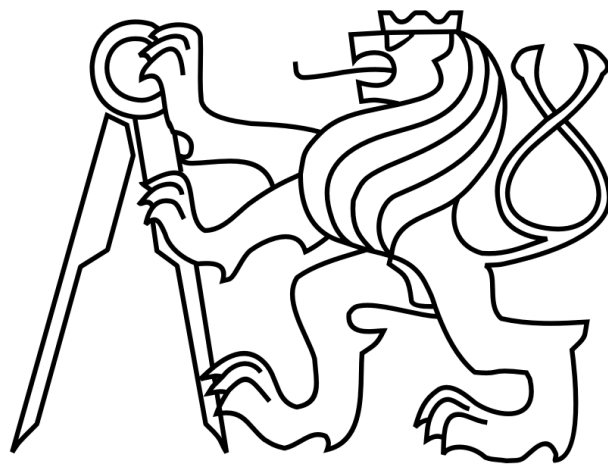


**CZECH TECHNICAL UNIVERSITY
IN PRAGUE**

**FACULTY OF NUCLEAR SCIENCES AND
PHYSICAL ENGINEERING**

Department of Physics

Experimental Nuclear and Particle Physics



Bachelor's thesis

Study of jet shape observables at RHIC

Author: Veronika Agafonova

Supervisor: RNDr. Jana Bielčíková, Ph.D.

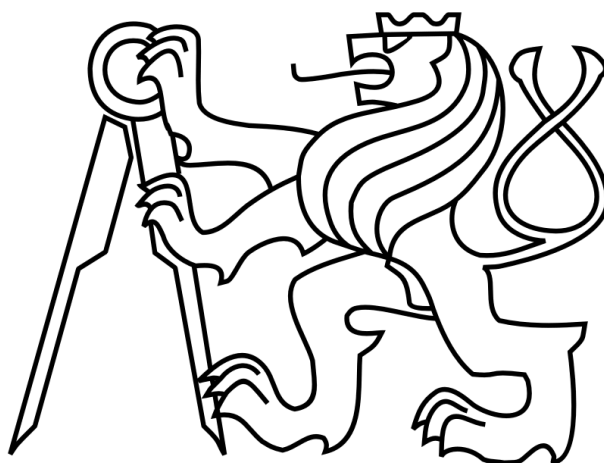
Prague, 2017

ČESKÉ VYSOKÉ UČENÍ TECHNICKÉ
V PRAZE

FAKULTA JADERNÁ A FYZIKÁLNĚ
INŽENÝRSKÁ

Katedra fyziky

Experimentální jaderná a částicová fyzika



Bakalářská práce

Studium tvaru jetů na urychlovači RHIC

Vypracovala: Veronika Agafonova

Školitel: RNDr. Jana Bielčíková, Ph.D.

Praha, 2017

Prohlášení

Prohlašuji, že jsem svou bakalářskou práci vypracovala samostatně a použila jsem pouze podklady (literaturu, projekty, SW atd.) uvedené v příloženém seznamu.

Nemám závažný důvod proti použití tohoto školního díla ve smyslu §60 Zákona č. 121/2000 Sb., o právu autorském, o právech souvisejících s právem autorským a o změně některých zákonů (autorský zákon).

V Praze dne

.....
podpis

Poděkování

Děkuji RNDr. Janě Bielčíkové, Ph.D. za vedení mé práce, trpělivost, pomoc s instalací Monte-Carlo generátoru JEWEL a provedení jazykové korektury této bakalářské práce.

Veronika Agafonova

Acknowledgement

I would like to thank my supervisor RNDr. Jana Bielčíková, Ph.D. for guiding this thesis, her willingness, patience, help with the JEWEL installation and providing language corrections.

Veronika Agafonova

Název práce: **Studium tvaru jetů na urychlovači RHIC**

Autor: Veronika Agafonova

Obor: Experimentální jaderná a částicová fyzika

Druh práce: Bakalářská práce

Vedoucí práce: RNDr. Jana Bielčíková, Ph.D.

Ústav jaderné fyziky AV ČR, v.v.i.

Konzultant: —

Abstrakt: Jádru-jaderné srážky při energiích dosažitelných na urychlovači RHIC v BNL v USA jsou ideálním prostředím ke studiu jaderné hmoty v extrémních podmínkách vysokých teplot a hustot energií. Jednou z nejdůležitějších sond této jaderné hmoty je studium produkce jetů. Cílem této bakalářské práce je diskutovat moderní algoritmy pro rekonstrukci jetů a popsat základní pozorovatelné popisující tvar jetů. Praktickou částí této práce je aplikace jetového algoritmu anti-kT a vybraných pozorovatelných popisujících tvar jetů na simulovaných datech v Monte-Carlo generátoru JEWEL při energii srážky 200 GeV v těžišťovém systému na nukleon-nukleonový pár dosažitelných na urychlovači RHIC.

Klíčová slova: jet, jetový algoritmus, RHIC, JEWEL, kvarkovo-gluonové plasma

Title: **Study of jet shape observables at RHIC**

Author: Veronika Agafonova

Abstract: The nuclear-nuclear collisions at energies attainable at the accelerator RHIC in BNL in the US are an ideal environment to study nuclear matter under extreme conditions of high temperature and energy density. One of the most important probes of the nuclear matter is study of the production of jets. The aim of this bachelor's thesis is to discuss modern algorithms of jet reconstruction and to describe the basic jet shape observables. The practical part of this thesis focuses on the application of the anti-kT algorithm and the chosen jet shape observables on the simulated data in the Monte-Carlo generator JEWEL at the center of mass energy of 200 GeV per nucleon-nucleon pair.

Key words: jet, jet algorithm, RHIC, JEWEL, quark-gluon plasma

Contents

1	Introduction to particle physics	1
1.1	Fundamental interactions	1
1.2	The Standard Model	2
1.2.1	Bosons	3
1.2.2	Fermions	3
2	Physics of nucleus-nucleus collisions	5
2.1	Quark-gluon plasma	5
2.2	Basic kinematic observables	6
2.3	Space-time evolution of nuclear collision	7
2.4	Centrality of the collision	10
2.4.1	The Glauber model	11
2.5	Tools for QGP studies	12
2.5.1	Anisotropic flow	12
2.5.2	Nuclear modification factor	14
2.5.3	Tomography of medium with hard probes	15
2.6	Actual results at STAR	17
3	RHIC and STAR	19
3.1	RHIC	19
3.2	STAR	20
3.2.1	Time Projection Chamber	20
3.2.2	Time Of Flight	22
3.2.3	Barrel Electro-Magnetic Calorimeter	23
3.2.4	Heavy Flavor Tracker	25
4	Algorithms of jet reconstruction	27
4.1	Introduction	27
4.2	Attributes of the ideal jet algorithm	28
4.2.1	Theoretical attributes of the ideal jet algorithm	28
4.2.2	Experimental attributes of the ideal jet algorithm	29
4.3	Cone jet finding algorithms	30
4.4	Cluster type jet finding algorithms	30
4.4.1	kT algorithm	31
4.4.2	Anti-kT algorithm	32
4.5	FastJet	34

5	JEWEL	37
5.1	Introduction	37
5.2	Physics of JEWEL	37
5.3	A simple model of the medium	39
6	Analysis of jets	43
6.1	Jet shapes	43
6.2	JEWEL simulation	45
6.2.1	Results for the simulation with medium	46
6.2.2	Results for the simulation without medium	50
7	Summary	57

List of Figures

1.1	The Standard Model of elementary particles with three generations of elementary particles, gauge bosons in the fourth column, and the Higgs boson in the fifth column [1].	2
2.1	A phase diagram of nuclear matter showing the temperature T dependence on the baryon chemical potential μ_B [2].	5
2.2	The dependence of the pseudorapidity η (blue) on the polar angle θ (red). As polar angle approaches zero, pseudorapidity becomes infinite.	6
2.3	A space-time view of a central collision of two heavy nuclei ($A + A$) in the Landau picture. a) Two nuclei approaching each other with relativistic velocities and zero impact parameter in the CMS frame. $\gamma = \frac{E_{cm}}{2m_N}$, where m_N is the nucleon mass. b) The slowing down of the nuclei with the next sticking together and producing particles. c) The light-cone representation of the high-energy hadron collision in the Landau picture. The shaded area is the particle production area.	7
2.4	A space-time view of a central collision of two heavy nuclei ($A + A$) in the Bjorken picture. a) The approach of two nuclei with ultra-relativistic velocities and zero impact parameters to each other in the CMS frame. b) Passage through each other and the next leaving the high excited matter with a small net baryon number between the nuclei, depicted in the shaded area. c) The light-cone representation of the high-energy hadron collision in the Bjorken picture. The shaded area is the area of forming the highly excited matter.	8
2.5	A space-time evolution of the relativistic heavy ion collision [3].	9
2.6	A schematic view of central, peripheral and ultra-peripheral collisions.	10
2.7	The measured charged particle multiplicity in Au+Au collision at $\sqrt{s_{NN}} = 200$ GeV by the STAR experiment together with correspondingly values of impact parameter b , number of participants N_{part} and fraction of geometrical cross-section σ/σ_{tot} [4].	11
2.8	Non-central relativistic/ultra-relativistic nucleus-nucleus collision. a) Transverse view. b) The almond shape of the participant region produces anisotropic transverse distribution. c) The almond shape of the participant region produces non-isotropic flows. \vec{p}_T is a transverse momentum vector [5], [6].	13
2.9	Azimuthal anisotropy v_2 of K_S^0 , Λ , Ξ and Ω as a function of transverse momentum, p_T , for (a) 0-80%, (b) 40-80%, (c) 10-40% and (d) 0-10% in Au+Au collisions at $\sqrt{s_{NN}} = 200$ GeV [7].	13

2.10	Nuclear modification factor R_{AA} as a function of p_T in different centrality classes of charge averaged pions, kaons, protons, π^0 and ϕ [7].	14
2.11	Nuclear modification factor R_{AA} of π^0 as a function of p_T for various 10%-wide centrality classes. [8].	15
2.12	a) Energy loss in the vacuum. b) Collisional energy-loss in QGP. c) Radiative energy loss in QGP. The thick solid line denotes the quark interacting with the randomly distributed colour sources (blue circles) and emitting gluon radiations.	16
2.13	Fully corrected distributions of $Y(p_{T,jet}^{ch})$ (upper panels) and its ratio I_{CP} (lower panels) for central and peripheral Au+Au collisions at $\sqrt{s_{NN}} = 200$ GeV, for anti-kT jets with $R = 0.4$ and $R = 0.5$ [9]. . .	17
2.14	The p_T spectrum of inclusive charged jets in central Au+Au collisions at $\sqrt{s_{NN}} = 200$ GeV for $R = 0.3$ corrected for background and detector effects [10].	18
3.1	Counter-rotating particle beams can cross at six intersections around the RHIC rings. Different detectors are/were located at each of the four intersection points [11].	19
3.2	STAR detector system [12].	20
3.3	The layout of the STAR Time Projection Chamber [13].	21
3.4	The energy loss measured in 200 GeV Au+Au collisions collected in 2014 at RHIC [14].	22
3.5	The momentum dependence of the particle mass resolution for a 100 ps time resolution for pions, kaons, protons and deuterons [15]. . . .	23
3.6	TOF particle identification from $1/\beta$ measured in 200 GeV Au+Au collisions collected in 2014 at RHIC [14].	23
3.7	Cross sectional views of the STAR detector. The Barrel EMC covers $ \eta \leq 1$. The BEMC modules slide in from the ends on rails which are held by aluminum hangers attached to the magnet iron between the magnet coils [16].	24
3.8	A side view of a STAR BEMC module. The image shows the location of the two layers of shower maximum detector at a depth of approximately 5 radiation length X_0 from the front face at $\eta = 0$ [16].	24
3.9	The Heavy Flavor Tracker. PXL - Pixel detector, IST - Intermediate Silicon Tracker, SSD - double-sided Silicon Strip Detector [17]. . . .	25
4.1	A schematic view of jets created in a heavy-ion collision [18].	27
4.2	An example of infrared sensitivity in cone jet clustering [19].	28
4.3	Collinear sensitivity in jet reconstruction [19].	29
4.4	A sample parton-level event generated with HERWIG Monte-Carlo generator of p+p collision clustered with kT and anti-kT algorithms [20].	32
4.5	Distribution of areas in di-jet events at the LHC for various jet finding algorithms (see legend). (a) passive area at parton level, (b) active area at hadron level including UE and pile-up [20].	33
4.6	The mean area in di-jet events at the LHC for various jet finding algorithms (see legend) [20].	34
4.7	The running times of kT jet-finder and FastJet implementations of the kT clustering algorithm versus the number of initial particles [21].	35

5.1	Schematic picture of extra emissions generated by the parton shower on top of a hard quark-gluon scattering effect described by a $2 \rightarrow 2$ matrix element [22].	38
5.2	Schematic picture of extra emissions in two well separated events. The re-scattering is only indicated for one parton [22].	38
5.3	Schematic picture of extra emissions and re-scatters taking place on comparable time scales [22].	39
5.4	Schematic picture of extra radiation and re-scattering where several momentum transfers can act coherently to induce an emission [22].	39
5.5	Centrality dependence of the intra-jet fragmentation function $D(z)$ in Pb+Pb collisions at $\sqrt{s_{NN}} = 2.76$ TeV for a jet radius $R = 0.4$, $p_{T,jet} > 100$ GeV/c and $\eta_{jet} < 2.1$ [23].	40
6.1	Fully corrected g (left) and $p_T D$ (right) distributions for the jet resolution parameter $R = 0.2$ in Pb-Pb collisions at $\sqrt{s_{NN}} = 2.76$ TeV at ALICE compared to PYTHIA Perugia 11 and JEWEL models [24].	43
6.2	Fully-corrected mean jet mass compared to PYTHIA Perugia 2011 and the jet quenching event generators (JEWEL and Q-PYTHIA) for anti-kT jets with $R = 0.4$ in the 10% most central Pb-Pb collisions [25].	44
6.3	The p_T spectrum of charged jets for resolution parameter $R = 0.2$ (upper one) and $R = 0.4$ (lower one) of data simulated with medium.	46
6.4	The radial moment distributions of data simulated with the resolution parameter $R = 0.2$ for two p_T intervals: $p_{T,jet} \in < 10; 20 >$ GeV/c (upper one) and $p_{T,jet} \in < 20; 30 >$ GeV/c (lower one).	47
6.5	The radial moment distributions of data simulated with the resolution parameter $R = 0.4$ for two p_T intervals: $p_{T,jet} \in < 10; 20 >$ GeV/c (upper one) and $p_{T,jet} \in < 20; 30 >$ GeV/c (lower one).	48
6.6	The momentum dispersion distributions of data simulated with the resolution parameter $R = 0.2$ for two p_T intervals: $p_{T,jet} \in < 10; 20 >$ GeV/c (upper one) and $p_{T,jet} \in < 20; 30 >$ GeV/c (lower one).	49
6.7	The momentum dispersion distributions of data simulated with the resolution parameter $R = 0.4$ for two p_T intervals: $p_{T,jet} \in < 10; 20 >$ GeV/c (upper plot) and $p_{T,jet} \in < 20; 30 >$ GeV/c (lower plot).	50
6.8	The p_T spectrum of charged jets for resolution parameter $R = 0.2$ (upper one) and $R = 0.4$ (lower one) of data simulated without medium.	51
6.9	The radial moment distributions of data simulated with the resolution parameter $R = 0.2$ for two p_T intervals: $p_{T,jet} \in < 10; 20 >$ GeV/c (upper one) and $p_{T,jet} \in < 20; 30 >$ GeV/c (lower one).	52
6.10	The radial moment distributions of data simulated with the resolution parameter $R = 0.4$ for two p_T intervals: $p_{T,jet} \in < 10; 20 >$ GeV/c (upper plot) and $p_{T,jet} \in < 20; 30 >$ GeV/c (lower plot).	53
6.11	The momentum dispersion distributions of data simulated with the resolution parameter $R = 0.2$ for two p_T intervals: $p_{T,jet} \in < 10; 20 >$ GeV/c (upper one) and $p_{T,jet} \in < 20; 30 >$ GeV/c (lower one).	54
6.12	The momentum dispersion distributions of data simulated with the resolution parameter $R = 0.4$ for two p_T intervals: $p_{T,jet} \in < 10; 20 >$ GeV/c (upper plot) and $p_{T,jet} \in < 20; 30 >$ GeV/c (lower plot).	55

Chapter 1

Introduction to particle physics

1.1 Fundamental interactions

There are four fundamental interactions between elementary particles: strong, weak, electromagnetic and gravitational. The Table (1.1) compares the basic properties of the interactions such as mediators (their spin and rest mass), range of the interactions and their relative forces.

Interaction	Mediator	Spin	Rest mass	Range	Relative force of the interaction
Strong	gluon g 8x	1^-	0	$\leq 10^{-15}$ m	~ 1
Electromagnetic	photon γ	1^-	0	∞	$\sim 10^{-2}$
Weak	W^\pm , Z^0	1^- , 1^+	80.41 GeV; 91.18 GeV	10^{-18} m	$\sim 10^{-7}$
Gravitational	graviton G	2^+	0	∞	$\sim 10^{-39}$

Table 1.1: Fundamental interactions together with their basic properties [26].

Strong interaction

The strong interaction binds together quarks in hadrons. It is also responsible for the forces that bind neutrons and protons in the nucleus of strong interacting particle with color charge. This interaction is mediated by eight massless gluons with the spin 1^- which carry the so called color charge. The strong interaction is described by Quantum Chromodynamics (QCD).

Electromagnetic interaction

The electromagnetic interaction is responsible for atomic structure, chemical reactions, the attractive and repulsive electromagnetic forces associated with electrically charged or magnetically polarized particles. Mediators of this interaction are mass-

less photons with the spin 1^- . This interaction is described by Quantum Electrodynamics (QED).

Weak interaction

The weak interaction is mediated by the W^\pm and Z^0 bosons, which act between quarks and leptons. Their rest masses are $M_{W^\pm} = 80.41 \text{ GeV}/c^2$ and $M_{Z^0} = 91.18 \text{ GeV}/c^2$. Using these masses, the typical range of the interaction can be estimated to $R \approx 2 \cdot 10^{-3} \text{ fm}$. In the low-energy limit the range of the interaction can be considered as negligible.

Gravitational interaction

The gravitational interaction acts on all particles and objects in Nature that have mass. As it can be seen from the Table 1.1 it is the weakest interaction from all. The mediator of this interaction is assumed to be a tensor particle *graviton* with the spin 2^+ and zero mass.

In the energy region about $5 \cdot 10^{14} \text{ GeV}$ the forces of interactions will be unified in one common force. The gravitational interaction is the only interaction that is not included in the Standard Model.

1.2 The Standard Model

The Standard Model is a theory which describes strong, weak and electromagnetic interactions between elementary particles (Figure 1.1).

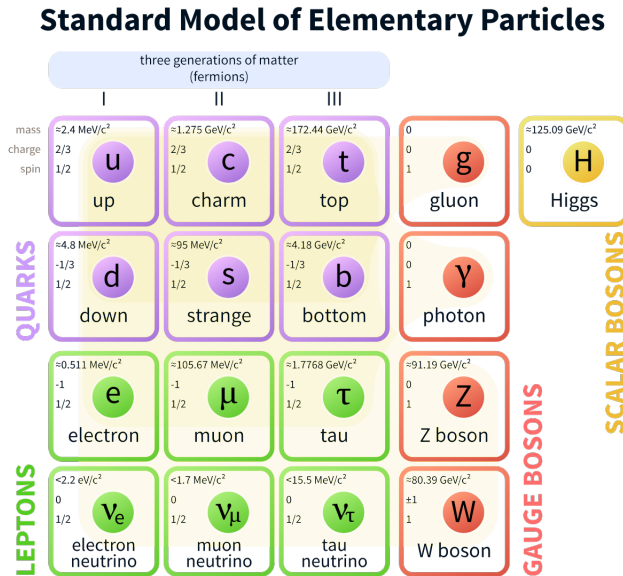


Figure 1.1: The Standard Model of elementary particles with three generations of elementary particles, gauge bosons in the fourth column, and the Higgs boson in the fifth column [1].

These particles are used in order to describe the structure of the matter observable in the Universe. They can be divided into 3 groups:

- Half-integer spin particles called *fermions*.
- Particles mediating the interactions between the fermions - spin 1 gauge *bosons*.
- Spin-0 *Higgs boson*, the quantum excitation of this Higgs field.

Every particle in Figure 1.1 can be characterized by its rest mass, electric charge and a set of quantum numbers (lepton, baryon).

1.2.1 Bosons

In the Standard Model gauge bosons are defined as force carriers that mediate the strong, weak, and electromagnetic fundamental interactions. Because of the spin 1 they do not follow the Pauli-exclusion principle, unlike fermions.

There are different types of bosons:

- *Photon* γ is the massless electroweak boson.
- Three massive *electroweak bosons* are W^+ , W^- and Z^0 . The weak interaction involving the W^\pm exclusively acts on left-handed particles and right-handed antiparticles. The electrically neutral Z^0 boson interacts with both left-handed particles and antiparticles.
- Eight massless *gluons*. They mediate the strong interactions between the quarks. Because gluons are carriers of color charge, they can also interact among themselves.

1.2.2 Fermions

As it was said before, fermions are the half-integer spin particles. Fermions in the Standard Model can be divided into quarks and leptons.

Quarks are fermions which form protons and neutrons in nucleus. Quarks are the only elementary particles in the Standard Model that undergo all of the four interactions. For every quark flavor there is a corresponding antiquark that differs from the quark only in that some of its properties have equal magnitude but opposite sign. There are three generations of quarks (two quarks in each generation). The first one consists from up and down quarks, the second one is formed by charm and strange quarks and the last one is formed by the top and bottom quarks. There is a quantum number to each flavor that has to be conserved in electromagnetic and strong interactions. They are S - strangeness, C - charm, \tilde{B} - beauty, T - truth, B - baryon number. In the weak interaction the electric charge and the baryon number B must be conserved.

Due to a phenomenon known as the *color confinement*¹, quarks are never directly observed or found isolated and they can be found only bound within hadrons. Hadrons are then divided into baryons and mesons. Baryons are hadrons made

¹**Color confinement** - the phenomenon that color charged particles (such as quarks) cannot be isolated singularly, and therefore cannot be directly observed.

up from three quarks ($p, n, \Lambda, \Lambda_c, \Delta^-, \Delta^{++} \dots$). Mesons are hadrons made up from two quarks ($\pi^+, K^-, D^-, B^-, B^s, J/\psi \dots$). Hadrons decay quickly ($\tau \approx 10^{-23} s$) into lighter products, if the conservation laws of their quantum numbers allow. Hadrons with longer lifetime cannot decay into the lighter products when the quantum numbers are concerned. That is why they decay via the weak interaction, which can change the quark flavor.

Leptons are fermions that does not undergo strong interactions. There are also six types of leptons, known as flavors, forming three generations. The first generation is *the electronic leptons*: electron and electron neutrino, the second one is *the muonic leptons*: muon and muon neutrino, the last one is *the tauonic leptons*: tau and tau neutrino. The *lepton numbers* L_e, L_μ, L_τ must be concerned in each generation separately.

Leptons are subject to the gravitational, electromagnetic (excluding neutrinos, which are electrically neutral) and the weak interactions. For every leptonic flavor there is a corresponding antilepton that differs from the lepton only in that some of its properties have equal magnitude but opposite sign.

Chapter 2

Physics of nucleus-nucleus collisions

2.1 Quark-gluon plasma

Nowadays many experiments do the research of nuclear matter called Quark-Gluon Plasma (QGP). QGP is a state of matter which exists at extremely high temperature and/or density when quarks and gluons are deconfined. Considering this, the Quark-Gluon Plasma can be found in the early Universe, at the center of compact stars and in the initial stage of collisions of heavy nuclei at high energies.

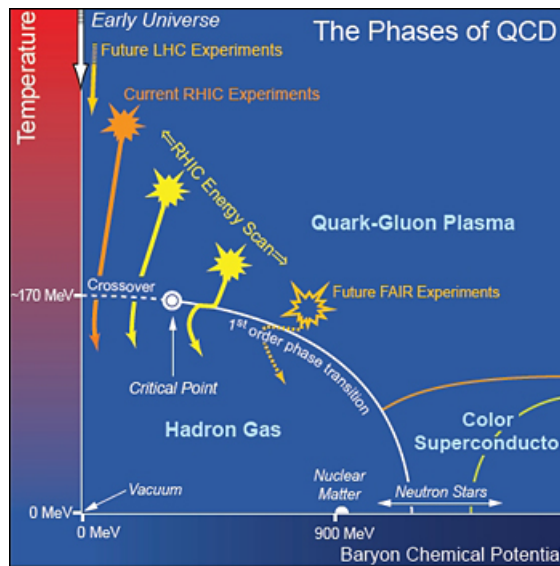


Figure 2.1: A phase diagram of nuclear matter showing the temperature T dependence on the baryon chemical potential μ_B [2].

In this thesis the focus will be only on heavy-ion collisions. Currently there are two large experimental facilities where high energy collisions are experimentally accessible. These are the Relativistic Heavy Ion Collider (RHIC) at Brookhaven National laboratory (BNL) and the Large Hadron Collider (LHC) at CERN which collide gold and lead respectively. At these colliders the initial temperature of the

QGP is expected to be higher than the critical temperature of the QCD phase transition ($T_c \sim 170$ MeV [5]). The nuclei are accelerated to ultra-relativistic speed and directed towards each other, creating a "fireball", in the rare event of a collision. The hadronisation starts when the QGP cools to the T_c temperature. Because of the confinement of colour degrees of freedom as latent degrees of freedom, a radical decrease in the entropy energy takes place. Hydrodynamic simulation predicts this fireball will expand under its own pressure, and cool while expanding. By carefully studying the elliptic flow, experimentators put the theory to test.

A typical phase diagram of QGP is depicted in the Figure 2.1, which shows the temperature T dependence on the baryon chemical potential μ_B . The temperature for the transition from the QGP to a hadron gas is ≈ 170 MeV for $\mu_B = 0$ and the phase boundary is predicted to be a smooth crossover down to a critical point below which the phase boundary becomes a first order phase transition.

2.2 Basic kinematic observables

In order to describe the properties of particles created in nuclear-nuclear collisions, it is good to define some variables accounting for relativistic effects. The first one is the *transverse momentum* p_T which is defined as

$$p_T = \sqrt{p_x^2 + p_y^2}. \quad (2.1)$$

Here, the p_x and p_y are the components of the three-momentum $\vec{p} = (p_x, p_y, p_z)$, the last component, p_z , is the component of the momentum along the beam axis (longitudinal momentum p_L).

The importance of the transverse momentum arises because momentum along the beamline may just be left over from the beam particles, while the transverse momentum is always associated with whatever physics happened at the collision vertex.

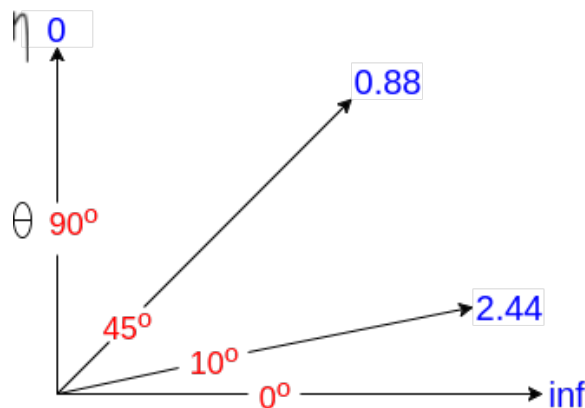


Figure 2.2: The dependence of the pseudorapidity η (blue) on the polar angle θ (red). As polar angle approaches zero, pseudorapidity becomes infinite.

The second variable is *rapidity*, y , a measure of velocity. Its definition is

$$y = \frac{1}{2} \ln \left(\frac{E + p_L}{E - p_L} \right). \quad (2.2)$$

However, in experimental particle physics the *pseudorapidity* η , defined as

$$\eta = -\ln\left(\tan\frac{\theta}{2}\right), \quad (2.3)$$

is usually used instead of rapidity. Here, θ is the angle between the particle three-momentum \vec{p} and the positive direction of the beam axis. In comparison to rapidity, pseudorapidity depends only on the polar angle of the particle's trajectory, and not on the energy of the particle. The dependence of the pseudorapidity on the polar angle is shown in the Figure 2.2.

The last variable which we mention here is the *center-of-mass energy*, CMS energy, which is defined as

$$\sqrt{s} = \sqrt{(E_1 + E_2)^2 - (p_1 + p_2)^2} \quad (2.4)$$

for the two colliding nucleons with momenta p_1, p_2 and energies E_1, E_2 .

$\sqrt{s_{NN}}$ is the CMS energy per nucleon. In case of a symmetric collision, the relation between previously defined CMS energies is $\sqrt{s_{NN}} = \sqrt{s}/A$, where A is a nucleon number.

2.3 Space-time evolution of nuclear collision

There are two space-time pictures of high-energy hadron collisions: Landau scenario and Bjorken scenario. Let us consider a central collision of two nuclei each having a mass number A in the center-of-mass frame with $\sqrt{s_{NN}} = E_{cm}$, as it is shown in the Figure 2.3. In this frame the nuclei are Lorentz-contracted, thus having a thicknesses of $d = 2R/\gamma$, where γ is the Lorentz factor.

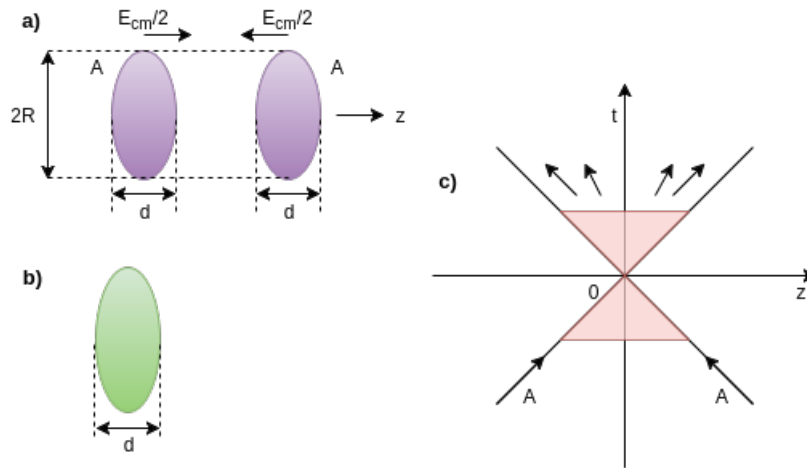


Figure 2.3: A space-time view of a central collision of two heavy nuclei ($A+A$) in the Landau picture. a) Two nuclei approaching each other with relativistic velocities and zero impact parameter in the CMS frame. $\gamma = \frac{E_{cm}}{2m_N}$, where m_N is the nucleon mass. b) The slowing down of the nuclei with the next sticking together and producing particles. c) The light-cone representation of the high-energy hadron collision in the Landau picture. The shaded area is the particle production area.

In the Landau picture, the colliding nuclei are considerably slowed down, producing particles, mainly within the thickness of nuclear matter. Afterwards, the hot system of particles, mainly baryons, undergoes a hydrodynamic expansion, mainly along the incident beam axis z . This situation is shown in the Figure 2.3c in the light-cone representation.

The second picture of high-energy hadron collisions is the Bjorken one (Figure 2.4), which replaces the Landau picture in the case of significantly higher incident energies of colliding nuclei. This picture is based on the parton model of hadrons and differs from the Landau picture in the existence of wee partons (gluons and sea-quarks) and the time expansion of the particle production.

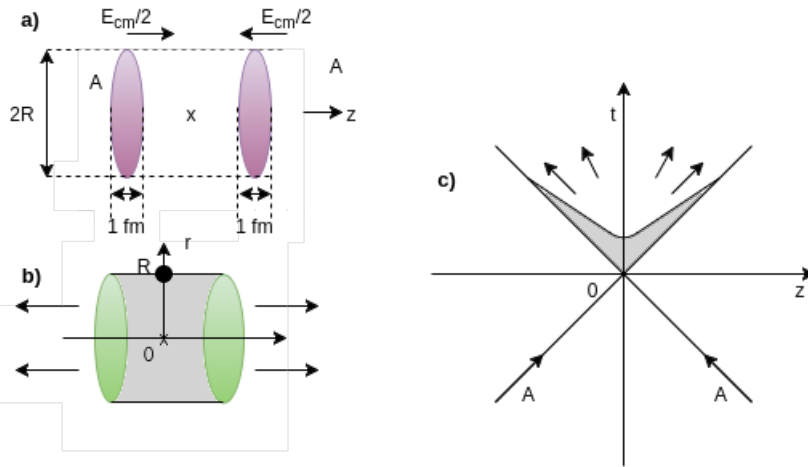


Figure 2.4: A space-time view of a central collision of two heavy nuclei ($A+A$) in the Bjorken picture. a) The approach of two nuclei with ultra-relativistic velocities and zero impact parameters to each other in the CMS frame. b) Passage through each other and the next leaving the high excited matter with a small net baryon number between the nuclei, depicted in the shaded area. c) The light-cone representation of the high-energy hadron collision in the Bjorken picture. The shaded area is the area of forming the highly excited matter.

As it is known, the nucleon is composed of valence quarks and wee partons. The wee partons may be regarded as a part of a coherent classical field created by the source of fast partons or the so called "colour glass condensate". As a consequence, it can be said that two incoming nuclei in the CMS frame before the collision wear the "fur coat of wee partons" [5]. The size of these wee partons is about 1 fm .

After the central collision of two beams occurs, a significant number of virtual quanta and a gluon coherent field configuration is excited (Figure 2.4(b)). During the de-excitation time, τ_{de} , which is typically about a fraction of 1 fm , the quanta are de-excited to real quarks and gluons. The τ_{de} , defined in the rest frame of each quantum, experiences Lorentz expansion and thus becomes $\tau = \tau_{de}\gamma$ in the CMS frame. This implies the so called *inside-outside cascade*, which is not taken into account in the Landau picture of the collisions. The essence of this phenomenon is that slow particles emerge first near the collision point, while the fast particles emerge last, far from the collision point.

As it was said earlier, in heavy ion collisions the Lorentz-contracted nuclei collide

with each other creating the so called fireball. This fireball undergoes different phases in its evolution, which are depicted in the space-time diagram. Since it is still not known how the relativistic collisions occur, Figure 2.5 is just a possible scenario of the relativistic collision.

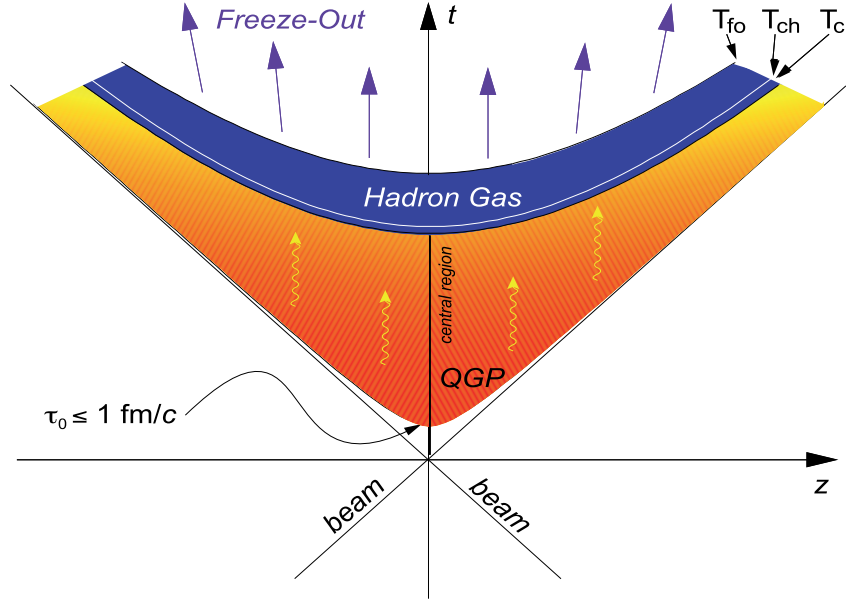


Figure 2.5: A space-time evolution of the relativistic heavy ion collision [3].

The evolution history of a relativistic nuclear collision, presented in the space-time diagram, can be divided into three stages which can be described as follows [5]:

- *Pre-equilibrium stage and thermalization:* $0 < \tau < \tau_0$

The central ultra-relativistic heavy nuclei collision is a process with large entropy production. There are two models of entropy production and subsequent thermalization: the incoherent and coherent models. In the first one, the incoherent sum of collisions of incoming partons produces semi-hard partons which afterwards interact with each other to form an equilibrated parton plasma. In the coherent collisions, the colour strings and ropes are formed after the impact. The process of entropy production and subsequent thermalization takes place before the characteristic proper time, τ_0 , and thus gives the initial condition of the hydrodynamic evolution of the system for $\tau > \tau_0$. The proper time τ_0 depends not only on the basic parton-parton cross-section, but also on the density of partons that were produced at the pre-equilibrium stage¹. The value of τ_0 is typically some fraction of 1 fm.

- *Hydrodynamical evolution and freeze out:* $\tau_0 < \tau < \tau_f$

At this stage the Eq. 2.5 of the energy-momentum tensor and baryon number conservation can be used to describe the expansion of the system.

$$\partial_\mu \langle T^{\mu\nu} \rangle = 0, \quad \partial_\mu \langle j_B^\mu \rangle = 0, \quad (2.5)$$

¹The pre-equilibrium stage is the state of matter for $0 < \tau < \tau_{de}$, where $\tau_{de} < \tau_0$.

In the case when the system can be approximated by a perfect fluid, the expectation values can be characterized by the local pressure P and the local density ϵ . Otherwise, the extra information, such as the viscosity or heat conductivity, etc., is required. The evolution of the thermalized QGP and its phase transition to the hadronic plasma take place at the $\tau_0 < \tau < \tau_f$ period until it reaches the freeze-out stage at $\tau = \tau_f$.

- *Freeze-out and post-equilibrium: $\tau_f < \tau$*

The freeze-out of the hadronic space, that is happening at $\tau = \tau_f$, is defined by a space-time hyper-surface. In this space-time hyper-surface the local thermal equilibrium is no longer maintained, since the mean free time of the plasma particles becomes larger than the time scale of the plasma expansion. There are two types of freeze-out: the chemical and the thermal freeze-out. The last one occurs at the temperature higher than the first one. After the chemical freeze-out the number of each species is frozen while the equilibrium in the phase-space is maintained. After the thermal freeze-out the kinetic equilibrium is no longer maintained. Over the time τ_f evolution of the medium ends, the distance between the hadrons increases, and therefore they leave the region of the collision. However, hadrons can still interact in a non-equilibrium way.

2.4 Centrality of the collision

In high-energy nuclear physics collisions may be classified according to their size of the overlapping area, which is described by the impact parameter b as a difference between the positions of the nuclei centers. There are three types of collisions: central or "head-on" collisions, peripheral and ultra-peripheral collisions (Figure 2.6). The first ones have $b \approx 0$, peripheral collisions have $0 < b < 2R$, and ultra-peripheral collisions have $b > 2R$, where the colliding nuclei are viewed as hard spheres with radius R .

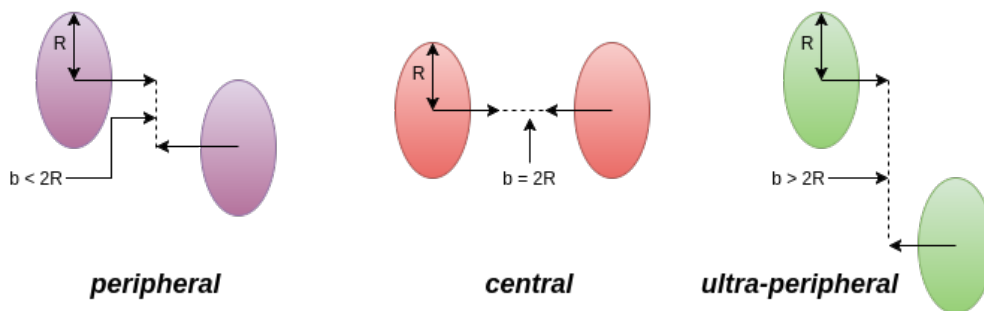


Figure 2.6: A schematic view of central, peripheral and ultra-peripheral collisions.

In heavy-ion collisions the centrality of the collision and the impact parameter cannot be directly experimentally measured. Thus, there are two ways to determine the centrality of the collision. The first is to measure the track multiplicity. The more central is the collision, the more nucleons participating in it turn to higher multiplicity and respectively the more tracks can be observed by the detector. Since the particle multiplicity is proportional to the energy released in the collision, one

can measure the particle multiplicity distribution for minimum bias collisions. Considering the high values of particle multiplicity correspond to central collisions and lower values correspond to more peripheral collisions, the multiplicity distribution could be used for centrality determination in a collision experiment. Figure 2.7 shows the charge particle multiplicity, N_{ch} , distribution used for the selection of collision centrality in a typical heavy-ion experiment [4].

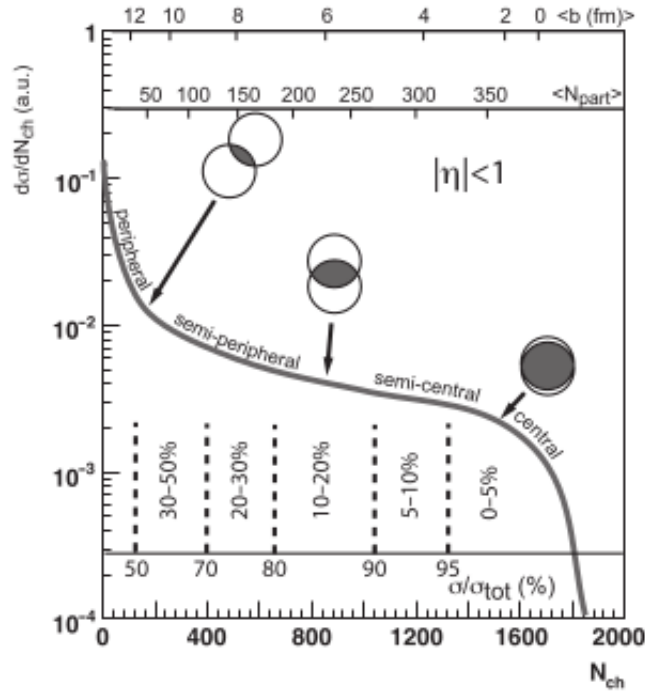


Figure 2.7: The measured charged particle multiplicity in Au+Au collision at $\sqrt{s_{NN}} = 200$ GeV by the STAR experiment together with correspondingly values of impact parameter b , number of participants N_{part} and fraction of geometrical cross-section σ/σ_{tot} [4].

Another way to determine the centrality is to measure the nucleons which do not participate in the collision. Such nucleons are called *spectators*. To measure spectators one uses e.g. special Zero Degree Calorimeters. Contrary to expectations, the number of the spectators for central and most peripheral collisions ~ 0 , since the nucleons in the colliding nuclei are not "kicked out" of the nuclei. Thus, they are not measured by ZDCs. Also, in the collision of deformed nuclei having different orientations there may be different amount of the spectators for the same impact parameter. The number of participant nucleons can be evaluated by the semi-classical Glauber model which will be briefly described below.

2.4.1 The Glauber model

The Glauber model is used for the description of high-energy nuclear reactions and also in evaluating the number of participant nucleons, N_{part} , and binary nucleon-nucleon collisions, N_{coll} . This model assumes that the nucleons travel along a

straight line and the nucleon-nucleon cross-section, σ_{NN}^{in} , to be the same as that in the vacuum. Due to these assumptions the Glauber model does not consider the secondary particle production and possible excitation of nucleons.

The number of participant nucleons N_{part} and the number of binary nucleon-nucleon collisions N_{coll} could be calculated using the following equations [5]:

$$N_{part}(b) = \int d^2\mathbf{s} T_A(\mathbf{s}) \left(1 - \exp^{-\sigma_{NN}^{in} T_B(\mathbf{s})}\right) + \int d^2\mathbf{s} T_B(\mathbf{s} - \mathbf{b}) \left(1 - \exp^{-\sigma_{NN}^{in} T_A(\mathbf{s})}\right), \quad (2.6)$$

$$N_{coll}(b) = \int d^2\mathbf{s} \sigma_{NN}^{in} T_A(\mathbf{s}) T_B(\mathbf{s} - \mathbf{b}), \quad (2.7)$$

where T_A is the thickness function defined as $T_A(s) = \int dz \rho_A(z, \mathbf{s})$, \mathbf{b} is the impact parameter, \mathbf{s} is the impact parameter of all the pairs of incident and target nucleons, z is the collision axis and ρ_A is the nuclear mass number density normalized to mass number A .

2.5 Tools for QGP studies

To measure elusive characteristics of quark-gluon plasma, a combination of different probes and observables is needed. Below we describe only anisotropic flow and nuclear modification factor. For a review we point the interested reader to [5].

2.5.1 Anisotropic flow

The anisotropic flow is an important probe of the earliest stages of the collision. Let one consider non-central collisions with the collision parameter $b \neq 0$. The overlap region has an "almond" shape as depicted in Figure 2.8. In this region the pressure gradient is expected to be steeper in the impact parameter direction and the collective flow will be developed in this direction resulting in momentum anisotropy of produced particles.

This momentum anisotropy can be quantified by a Fourier expansion of the measured momentum distribution of particles as follows:

$$E \frac{d^3N}{d^3p} = \frac{d^2N}{2\pi p_T dp_T dy} \left(1 + \sum_{n=1}^{\infty} 2v_n \cos[n(\phi - \Phi_r)]\right), \quad (2.8)$$

where ϕ is the azimuthal angle of the particle and Φ_r is the azimuthal angle of the reaction plane in the laboratory frame. The coefficients v_n can be calculated as:

$$v_n = \langle \cos[n(\phi - \Phi_r)] \rangle. \quad (2.9)$$

The first two coefficients are called the direct (v_1) and elliptic (v_2) flow respectively.

Similarly as the impact parameter the reaction plane angle cannot be directly measured and has to be estimated from the detected particles (the so called event plane).

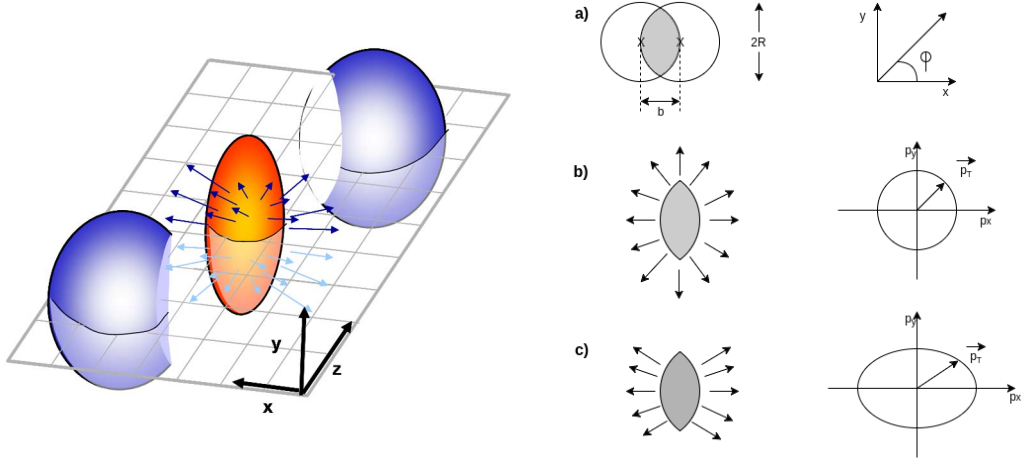


Figure 2.8: Non-central relativistic/ultra-relativistic nucleus-nucleus collision. a) Transverse view. b) The almond shape of the participant region produces anisotropic transverse distribution. c) The almond shape of the participant region produces non-isotropic flows. \vec{p}_T is a transverse momentum vector [5], [6].

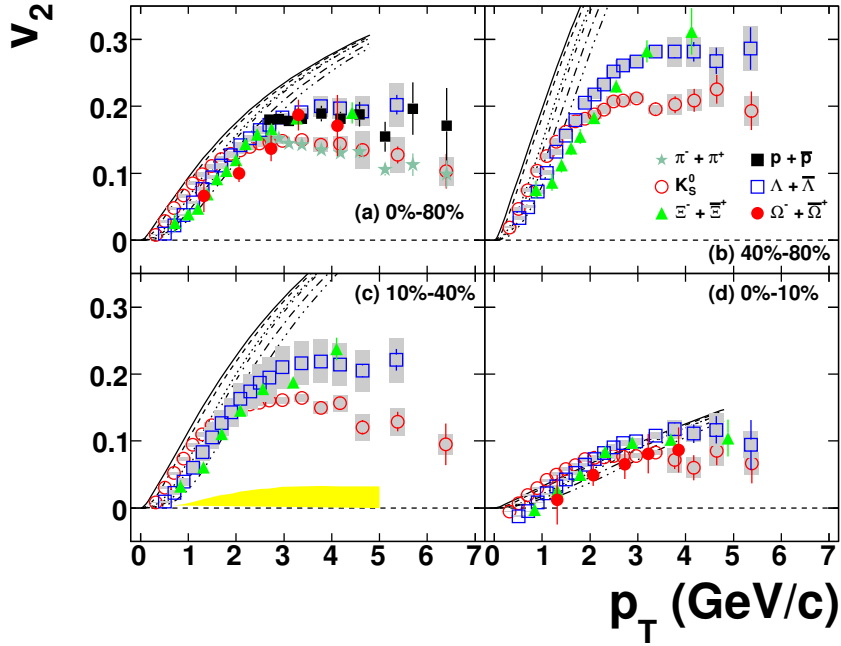


Figure 2.9: Azimuthal anisotropy v_2 of K_S^0 , Λ , Ξ and Ω as a function of transverse momentum, p_T , for (a) 0-80%, (b) 40-80%, (c) 10-40% and (d) 0-10% in Au+Au collisions at $\sqrt{s_{NN}} = 200$ GeV [7].

In case the angular distribution is dominated by the anisotropic flow (Eq. 2.9), the azimuthal angle of the event plane can be determined independently for each Fourier

harmonic of the flow:

$$\Phi_r^{(n)} = \frac{1}{n} \left(\tan^{-1} \frac{\sum_i \omega_i \sin n\phi_i}{\sum_i \omega_i \cos n\phi_i} \right), \quad (2.10)$$

where the ω_i is the weight of the i th particle. Typically p_T of particle is used as a weight.

The large value of the elliptic flow indicates the presence of the strongly interacting matter in the collision. Figure 2.9 shows the dependence of azimuthal anisotropy for of K_S^0 , Λ , Ξ and Ω as a function of p_T for different centralities in Au+Au collisions at $\sqrt{s_{NN}} = 200$ GeV. As it can be seen, the system agrees better with the ideal hydrodynamic model (black line) for more central collisions. Also, there are negative values of v_2 for the heavier hadrons at the lowest observed p_T in the most central Au+Au collisions (right bottom graph).

2.5.2 Nuclear modification factor

The nuclear modification factor, R_{AA} , is constructed to be a measure of particle production or jet production in nuclear medium. It is defined as:

$$R_{AA}(p_T) = \frac{\sigma_{AA}(p_T)}{\langle N_{binary} \rangle \sigma_{NN}(p_T)}, \quad (2.11)$$

where $\sigma_{AA}(p_T)$ and $\sigma_{NN}(p_T)$ are the p_T distributions from AA and p-p collisions respectively, $\langle N_{binary} \rangle$ is the number of binary nucleon-nucleon collisions, which in the experiment is estimated for central and peripheral collisions from trigger cross-section.

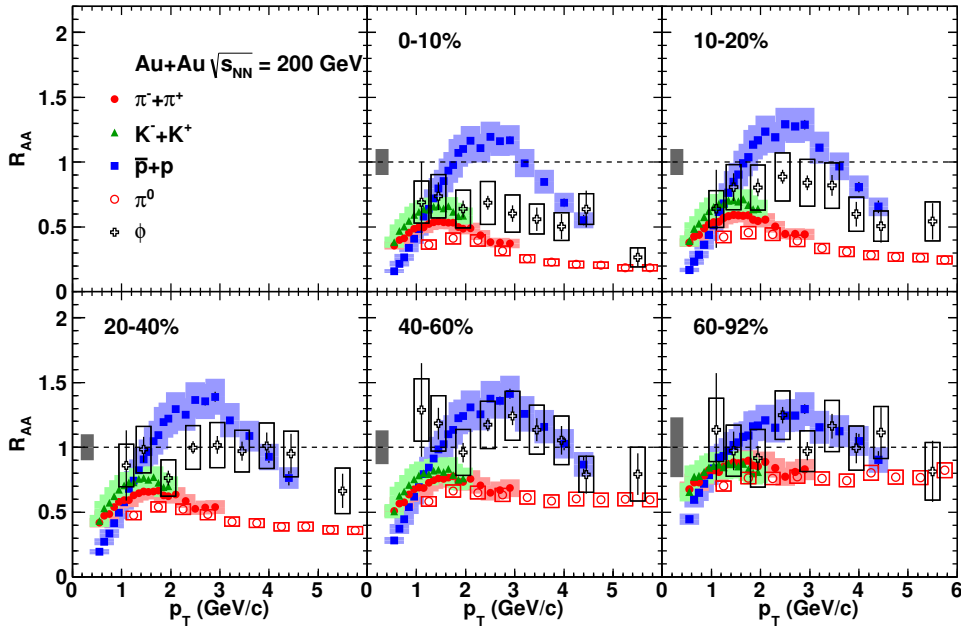


Figure 2.10: Nuclear modification factor R_{AA} as a function of p_T in different centrality classes of charge averaged pions, kaons, protons, π^0 and ϕ [7].

Figure 2.10 compares the nuclear modification factor, R_{AA} , for pions, kaons, and protons, π^0 and ϕ in different centrality classes in Au+Au collisions. The R_{AA} data are limited above by the p+p data. The pions and kaons exhibit a suppression pattern in the R_{AA} . Additionally, the suppression decreases as the collisions become more peripheral. There is no suppression in the intermediate p_T region for the proton R_{AA} , but it reaches its maximum value above unity between 2-3 GeV/c.

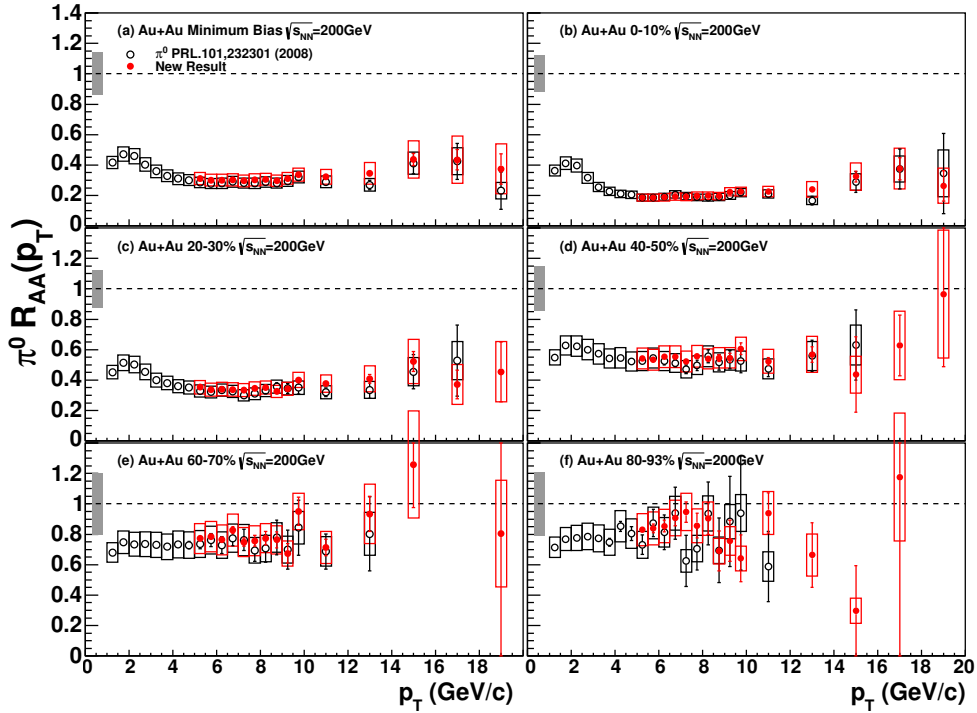


Figure 2.11: Nuclear modification factor R_{AA} of π^0 as a function of p_T for various 10%-wide centrality classes. [8].

The PHENIX experiment expands the measurement up to 20 GeV as it is shown in Figure 2.11. Black circles are results from [27] and red circles are the new results from [8]. As it can be seen, the suppression for the central collisions remained constant for big p_T . With the growth of centrality the suppression becomes lower.

2.5.3 Tomography of medium with hard probes

A fast charged particle, such as for example an electron passing through matter, loses its energy. There are two ways of losing energy. The first one is the collisional source. It is connected with the two-body scattering of the fast particle with the matter constituents. The second one is the radiative source, which is due to the Bremsstrahlung during the collisions with the matter. This type of energy loss is dominant at the high energies.

Let one has a high-energy parton created by a hard collision in the initial stage of a nucleus-nucleus collision. There will be three following energy losses:

1. Since the fast parton is a colour object, it forms a colour flux tube. After the parton deceleration, an extra tube forms by the kinetic energy loss. Particle

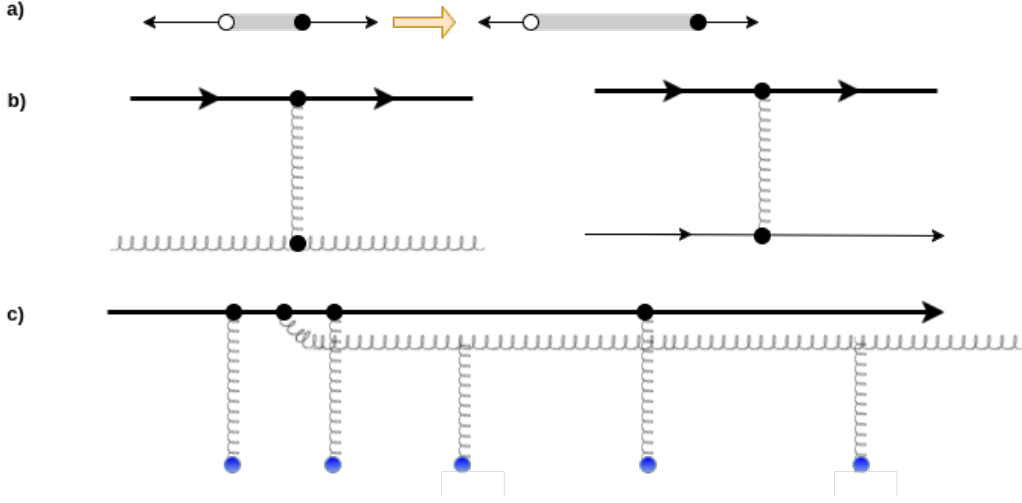


Figure 2.12: a) Energy loss in the vacuum. b) Collisional energy-loss in QGP. c) Radiative energy loss in QGP. The thick solid line denotes the quark interacting with the randomly distributed colour sources (blue circles) and emitting gluon radiations.

creation releases the energy stored in the tube, which is observed as jets. The energy loss is then:

$$-\frac{dE}{dx} \sim K = 0.9 \text{ GeV/fm}, \quad (2.12)$$

where K is the string tension of the flux tube (Figure 2.12a).

2. The collisions with the soft particles in QGP can affect the high-energy jets created in the initial stage of nucleus-nucleus collisions. Figure 2.12b shows the scattering process assessing this collisional energy loss. The thick solid lines represent a high-energy quark. The energy loss in this case can be calculated via:

$$-\frac{dE}{dx} \approx C_2 \pi \alpha_s^2 T^2 \left(1 + \frac{N_f}{6} \right) \ln \left(a \frac{ET}{\omega_D^2} \right). \quad (2.13)$$

In this equation a is a constant of $\mathcal{O}(1)$, C_2 is the quadric Casimir invariant having a value of $4/3$ for the quark and 3 for the gluon, ω_D is the Debye screening mass, T is the kinetic energy [5].

3. Figure 2.12c shows the radiative energy loss with the non-Abelian LPM-effect². It is more efficient mechanism than the collisional energy loss described above. In the relativistic nuclear-nuclear collisions the high-energy partons interact with soft plasma constituents only a few times before leaving the hot zone. Therefore, the plasma in these collisions is relatively thin. It is also expanding as a function of time. Taking these facts into account, the formula for this energy loss source is:

$$\Delta E(L) \sim \frac{9}{4} C_2 \pi \alpha_s^3 \left(\frac{dN_g}{A_T dy} \right) L \ln \left(\frac{2E}{\omega_D^2 L} + \frac{3}{\pi} + \dots \right), \quad (2.14)$$

²LPM or Landau - Pomeranchuk - Migdal effect is reduction of the Bremsstrahlung and pair production cross sections at high energies or high matter densities [5].

where $A_T = \pi R^2$ is the transverse size of nucleus, L is the path length of the jet in medium, dN_g/dy is the number of gluons produced in the central rapidity region.

The aim of studying the types of energy losses is to solve the detailed dimensional and temporal structure of quark-gluon plasma. These studies are also called *jet tomography* and can be applied not only for the fast parton, but also for the heavy quarks and high-energy photons.

2.6 Actual results at STAR

The summary of recent experimental results from STAR is shown in Figures 2.13 and 2.14. In Figure 2.13 the upper panels show the fully corrected distributions of $Y(p_{T,jet}^{ch})$ for central and peripheral Au+Au collisions at $\sqrt{s_{NN}} = 200$ GeV for anti-kT jets with $R = 0.4$ and $R = 0.5$. The lower panels shows the ratio of $Y(p_{T,jet}^{ch})$ in central to peripheral distributions (I_{CP}). The I_{CP} is calculated for so called "recoil jets" which fly at an angle 180° from the trigger hadron. The recoil jets are strongly suppressed in the region $p_{T,jet}^{ch} > 10$ GeV/c with less suppression for $R = 0.5$ than for $R = 0.4$. Charged jets were reconstructed with the anti-kT algorithm (Subsection 4.4.2) with jet resolution parameters $R = 0.2$ and $R = 0.5$ for jet constituents having $p_T > 0.2$ GeV/c. As it can be seen, the PYTHIA results are higher than results for central and peripheral collisions for both graphs. For the resolution parameter $R = 0.5$ (right) the distributions of $Y(p_{T,jet}^{ch})$ for central and peripheral collisions agree better with each other in comparison to the distributions with $R = 0.4$ (left). At low p_T the I_{CP} is close to one, but for $p_T > 10$ GeV the significant jet yield suppression $I_{CP} \approx 0.2$ can be observed in central Au+Au collisions.

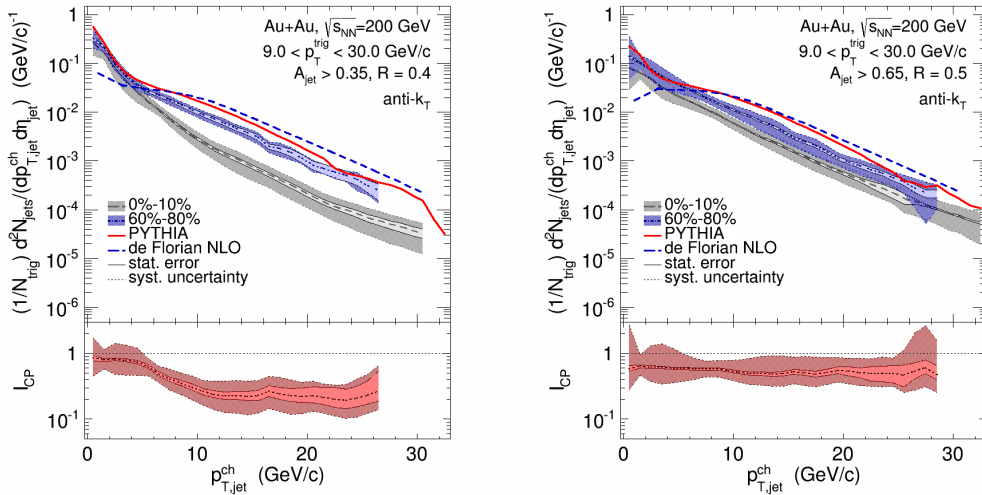


Figure 2.13: Fully corrected distributions of $Y(p_{T,jet}^{ch})$ (upper panels) and its ratio I_{CP} (lower panels) for central and peripheral Au+Au collisions at $\sqrt{s_{NN}} = 200$ GeV, for anti-kT jets with $R = 0.4$ and $R = 0.5$ [9].

Figure 2.14 shows the p_T spectrum of inclusive charged jets in 0-10% central Au+Au collisions at $\sqrt{s_{NN}} = 200$ GeV for the resolution parameter $R = 0.3$ corrected for background and detector effects. Jets were reconstructed using the charged tracks with $p_T \geq 200$ MeV/c recorded by the STAR Time Projection Chamber (TPC) during the RHIC data taking period in 2011 (Run11). For jet reconstruction the anti-kT algorithm (see Subsection 4.4.2) implemented in the FastJet software package (cf. Section 4.5) was used. In order to reduce the combinatorial background, a cut on the jet area $A > 0.2$ in case of $R = 0.3$ was applied.

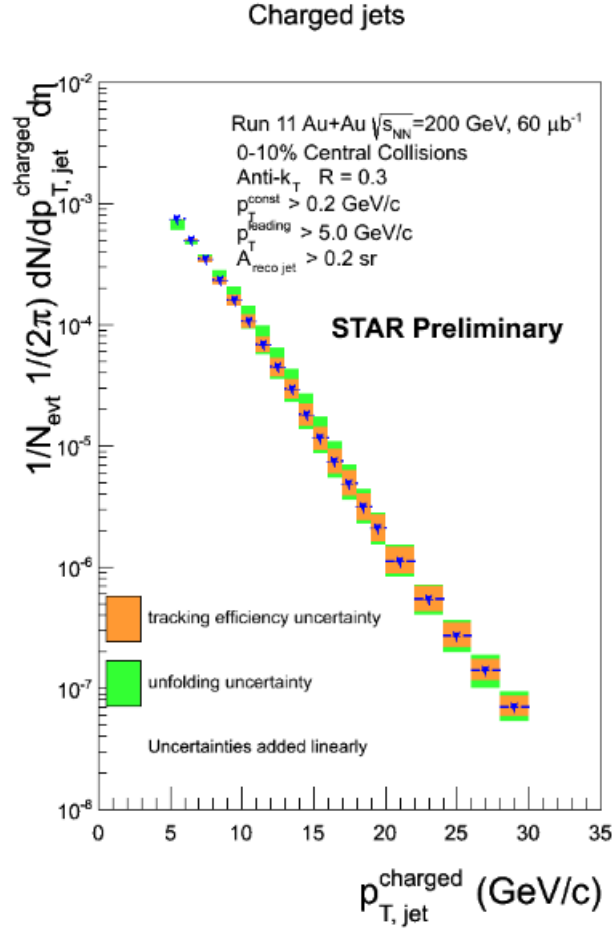


Figure 2.14: The p_T spectrum of inclusive charged jets in central Au+Au collisions at $\sqrt{s_{NN}} = 200$ GeV for $R = 0.3$ corrected for background and detector effects [10].

Chapter 3

RHIC and STAR

3.1 RHIC

The **R**elativistic **H**eavy **I**on **C**ollider (RHIC) is situated at Brookhaven National Laboratory. It was built inside a 2.4 mile circumference underground tunnel. It was the first machine in the world capable of colliding heavy ions. RHIC uses mainly ions of gold, because its nucleus is densely packed with particles. The two beams of gold ions travelling at near the speed of light collide "head-on" at six intersections where different experiments are situated. Initially, there were two large experiments at RHIC: PHENIX and STAR, and two small ones: BRAHMS and PHOBOS, as it is shown in Figure 3.1. Experiments BRAHMS and PHOBOS finished data taking 10 years ago. PHENIX measured last data in 2016 and now is being transformed to a new sPHENIX experiment. At present time STAR is therefore the only running experiment at RHIC that collects data. For this reason, it will be described below in more details.

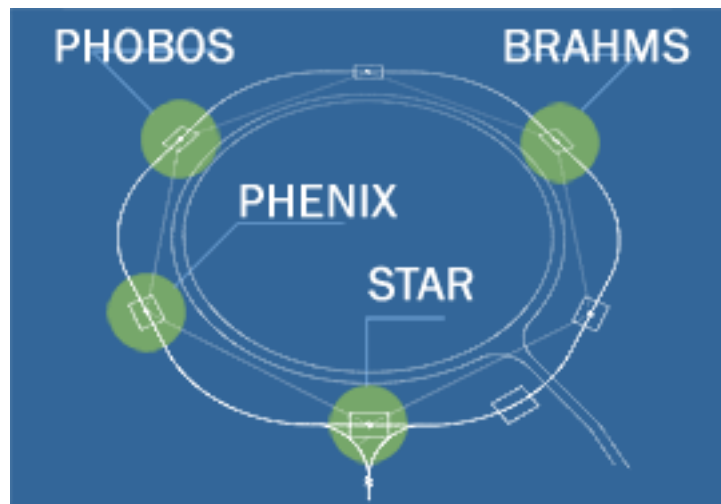


Figure 3.1: Counter-rotating particle beams can cross at six intersections around the RHIC rings. Different detectors are/were located at each of the four intersection points [11].

3.2 STAR

The **Solenoidal Tracker At RHIC (STAR)** is designed to detect charged and neutral particles that arise as a result of the interaction of relativistic heavy ions or protons. It is a large detector system built at the 6 o'clock intersection point of the two RHIC rings. Figure 3.2 shows the STAR detector system. In each collision of ultra-relativistic ions a large number of particles are produced. Thus, in central Au+Au collisions, more than 1000 primary particles are formed. In addition, when primary particles interact with the detector material and short-lived particles decay, additional secondary particle fluxes arise. All these particles must be identified and their trajectories determined.

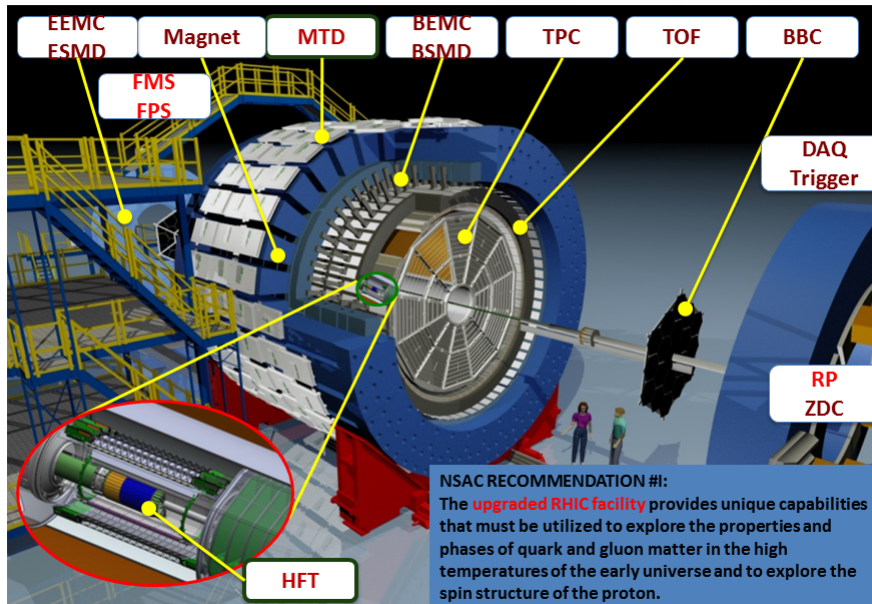


Figure 3.2: STAR detector system [12].

The **T**ime **P**rojection **C**hamber (TPC) is the main part of the system to measure charged particle tracks after collisions. The **B**arrel and **E**ndcap **E**lectro-**M**agnetic Calorimeter (BEMC and EEMC) allow to measure hadronic and photonic energy deposition in the calorimeter towers. The **B**eam-**B**eam **C**ounter (BBC), **V**ertex **P**osition **D**etector (VPD) and **Z**ero-**D**egree **C**alorimeter (ZDC) are used to monitor collision luminosity and beam polarimetry. The **T**ime **O**f **F**light detector (TOF) of STAR is designed for improvement of direct identification of hadrons.

The most important parts of the STAR detector system for studying jets are BEMC, TPC, HFT and TOF. Therefore, a more detailed description is given below.

3.2.1 Time Projection Chamber

The TPC is the central part of the STAR detector system. It is a cylindrical detector with 4 m in diameter and 4.2 m in length built around the beam-line. In a high- \sqrt{s}

heavy ion collisions many particles are produced. Electrically charged particles are deflected by the STAR magnet in a helical motion. The TPC is able to record those tracks, measure their momenta and identify particles by their ionization energy loss (dE/dx), which is calculated using the Bethe-Bloch formula

$$\frac{dE}{dx} = 4\pi N_A r_e^2 m_e c^2 z^2 \frac{Z}{A\beta^2} \left(\frac{1}{2} \ln \frac{2m_e c^2 \beta^2 \gamma^2 T_{max}}{I^2} \right) - \beta^2 - \frac{\delta}{2} - 2\frac{C}{Z}, \quad (3.1)$$

where N_A is the Avogadro number, r_e is classical electron radius, m_e is the mass of the particle that losses energy, z is the charge of the incoming particle, ρ is material density, T_{max} is maximum energy transfer in a single collision, Z and A are the atomic number and nucleus weight respectively, δ and C are the density and shell corrections, I is the mean excitation energy.

The TPC acceptance covers 2π in azimuthal angle ϕ and approximately from -1.3 to $+1.3$ in pseudo-rapidity η . Figure 3.3 shows the layout of the STAR Time Projection Chamber. It consists of a central membrane, an outer and inner field cage and two end-cap planes. The empty space between the central membrane and two end-caps is filled with gas. When charged particles pass through the TPC gas, the ionized secondary electrons drift toward the two end-caps in the uniform electric field provided by the central membrane and the end-caps. The drifting electrons are collected at the end-caps.

Figure 3.4 shows the track energy loss measured by the TPC in 200 GeV Au+Au collisions with the different particle species associated to the observed bands.

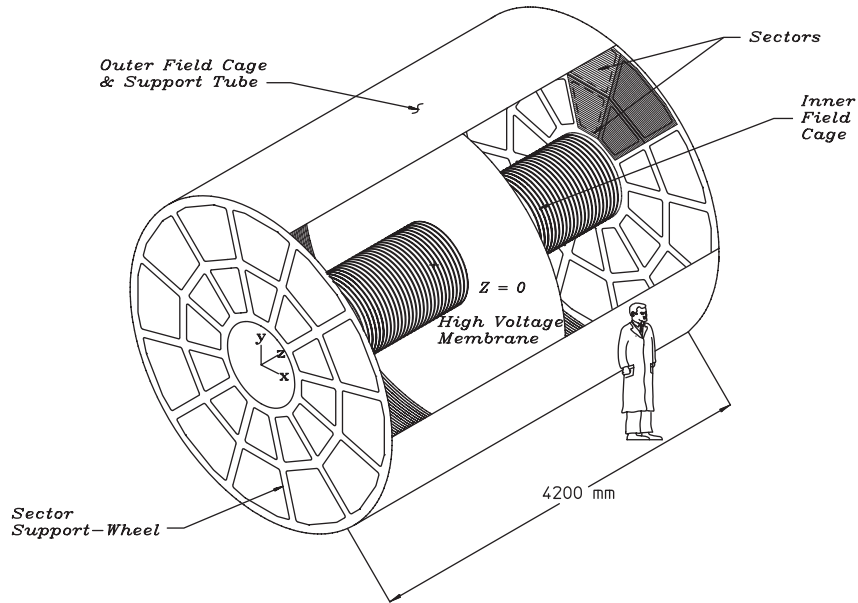


Figure 3.3: The layout of the STAR Time Projection Chamber [13].

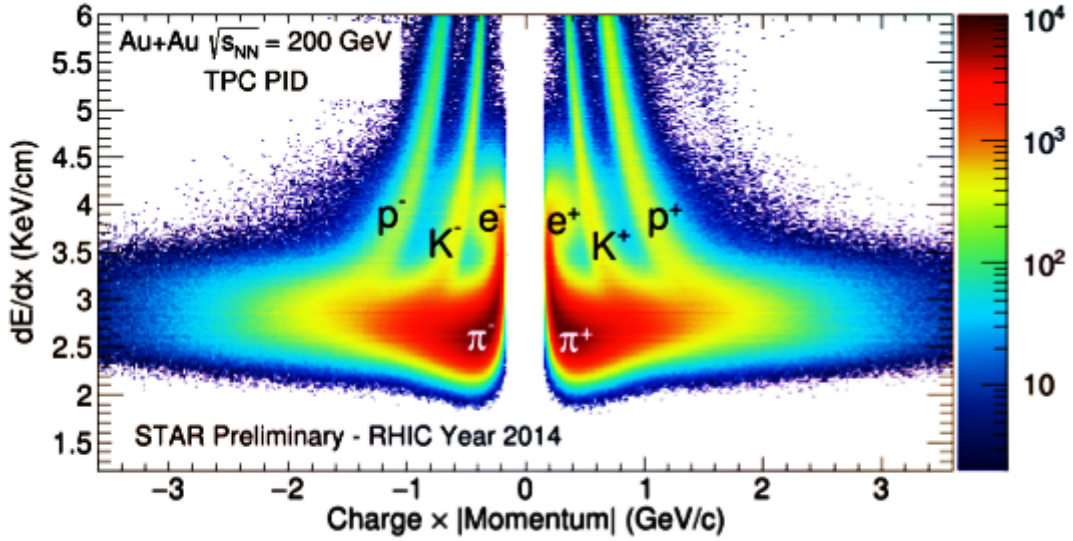


Figure 3.4: The energy loss measured in 200 GeV Au+Au collisions collected in 2014 at RHIC [14].

3.2.2 Time Of Flight

The **Time Of Flight** (TOF) system is located around the TPC as can be seen in Figure 3.2. The TOF measures time intervals with a specific precision. The "start" time is measured by the Vertex Position Detectors and the "stop" time is measured by the TOF. The difference, Δt , between these times is the time of the flight of the particle. Using the data from the TPC the inverse velocity $1/\beta$ for each track and the particle mass M can be calculated as

$$\frac{1}{\beta} = c \frac{\Delta t}{s}, \quad (3.2)$$

$$M = p \sqrt{\frac{1}{\beta^2} - 1}, \quad (3.3)$$

where s is the total path length, p is the momentum and c is the speed of light.

Figure 3.5 shows the momentum dependence of the particle mass resolution for a 100 ps time resolution for pions, kaons, protons and deuterons. The upper line in the pair shows the dependence of $M + \Delta M$ versus the momentum. The lower line demonstrates the $M - \Delta M$ dependence on the momentum. Figure 3.6 shows an example of particle identification with the TOF from 2014 Au+Au collisions at the top RHIC energy.

Such TOF system can provide direct K , p or π identification up to momenta $p \sim 1.7$ GeV/c, proton identification up to $p \sim 2.6$ GeV/c, deuteron identification out to $p \sim 4$ GeV/c [15]. It can be also seen from this figure that with the increasing momentum pions are the first particles leading to a significant background in the proton identification and the first background to deuteron identification.

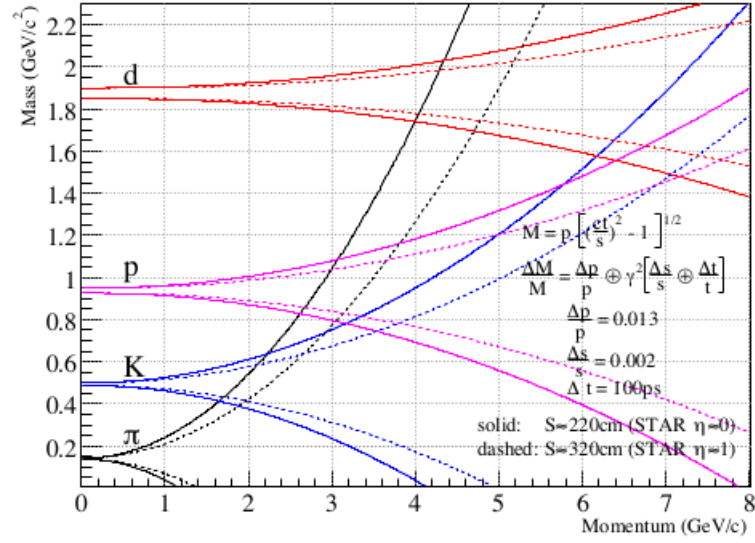


Figure 3.5: The momentum dependence of the particle mass resolution for a 100 ps time resolution for pions, kaons, protons and deuterons [15].

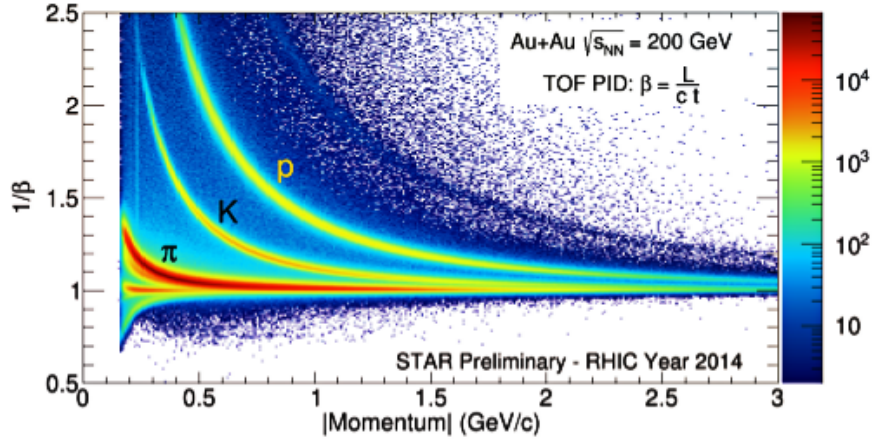


Figure 3.6: TOF particle identification from $1/\beta$ measured in 200 GeV Au+Au collisions collected in 2014 at RHIC [14].

3.2.3 Barrel Electro-Magnetic Calorimeter

The **Barrel Electro-Magnetic Calorimeter (BEMC)** allows STAR to trigger on and study high- p_T processes, e.g. jets, heavy quarks, because of its acceptance that is equal to that of the TPC for full length tracks (Figure 3.7).

The BEMC is located inside the aluminium coil of the STAR solenoidal magnet. The front face of the BEMC located at a radius of 220 cm is parallel to the axis of the beam.

The BEMC is a sampling calorimeter which includes a total of 120 calorimeter

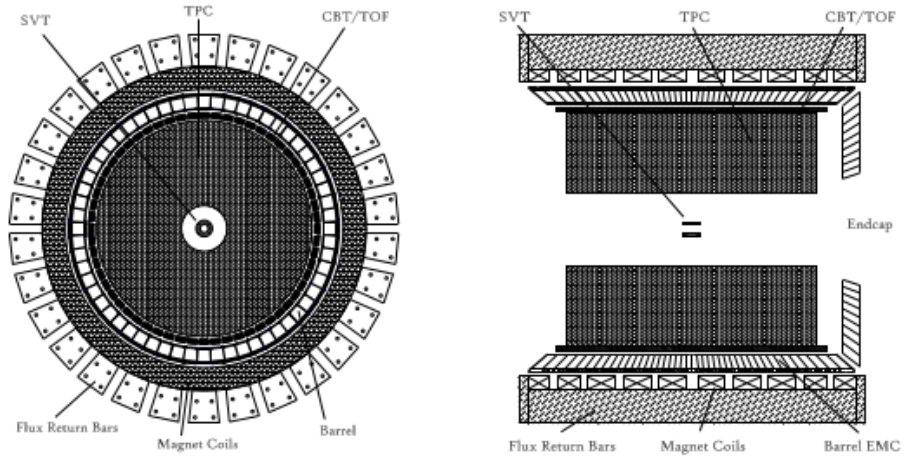


Figure 3.7: Cross sectional views of the STAR detector. The Barrel EMC covers $|\eta| \leq 1$. The BEMC modules slide in from the ends on rails which are held by aluminum hangers attached to the magnet iron between the magnet coils [16].

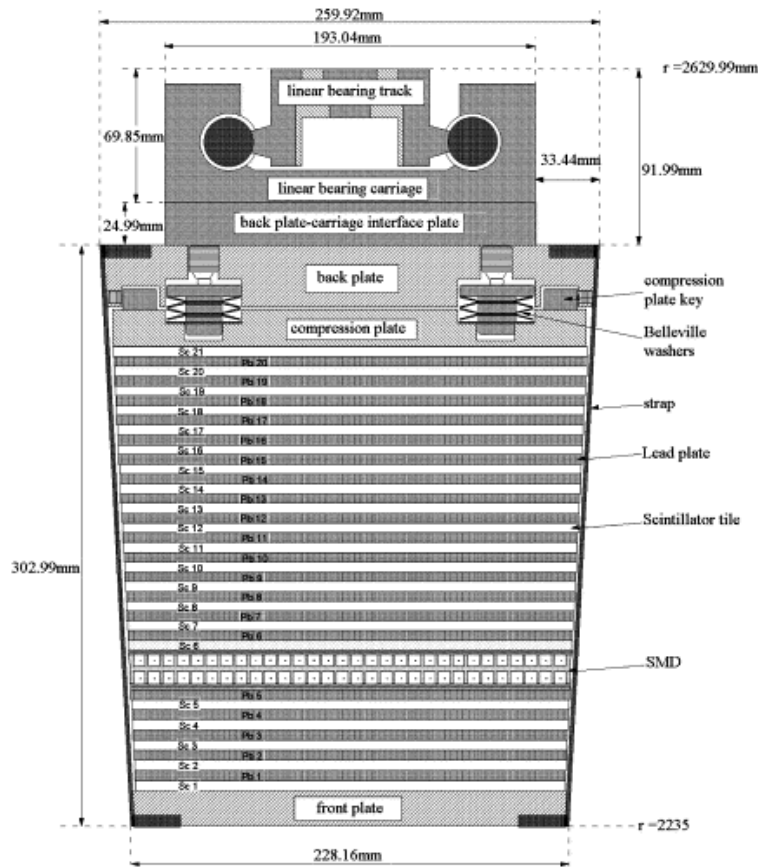


Figure 3.8: A side view of a STAR BEMC module. The image shows the location of the two layers of shower maximum detector at a depth of approximately 5 radiation length X_0 from the front face at $\eta = 0$ [16].

modules. The core of each module consists of a lead-scintillator stack and shower maximum detectors. There are 20 layers of a 5 mm thick lead, 19 layers of a 5 mm thick scintillator and 2 layers of a 6 mm thick scintillator [16]. The core structure is held together by compression of a combination of 30 straps and a system of bolts and spring washers between the back plate and the compression plate. The friction between individual layers guarantees the calorimeter stack's stability. An end-view of a module showing the mounting system and the compression components is demonstrated in Figure 3.8.

3.2.4 Heavy Flavor Tracker

The Heavy Flavor Tracker (HFT) (Figure 3.9) is a new tracker of STAR installed in the 2014. After reaching very successfully its goals in 2016 it was removed. The HFT enables precision tracking measurements of heavy quarks, like B^0 or D^0 , at low momentum where the particle production is most sensitive to the bulk medium created in heavy ion collisions. This allows to distinguish the decay vertices of heavy flavor particles from primary vertices and significantly reduces combinational background, which yields cleaner measurements with a higher level of significance.

The HFT consists of two detectors: a silicon pixel detector and an intermediate silicon tracker. The minimal radius of the HFT is only 2.5 cm. Therefore it tightly surrounds the beam pipe that has to be thinner than in any other place at RHIC.

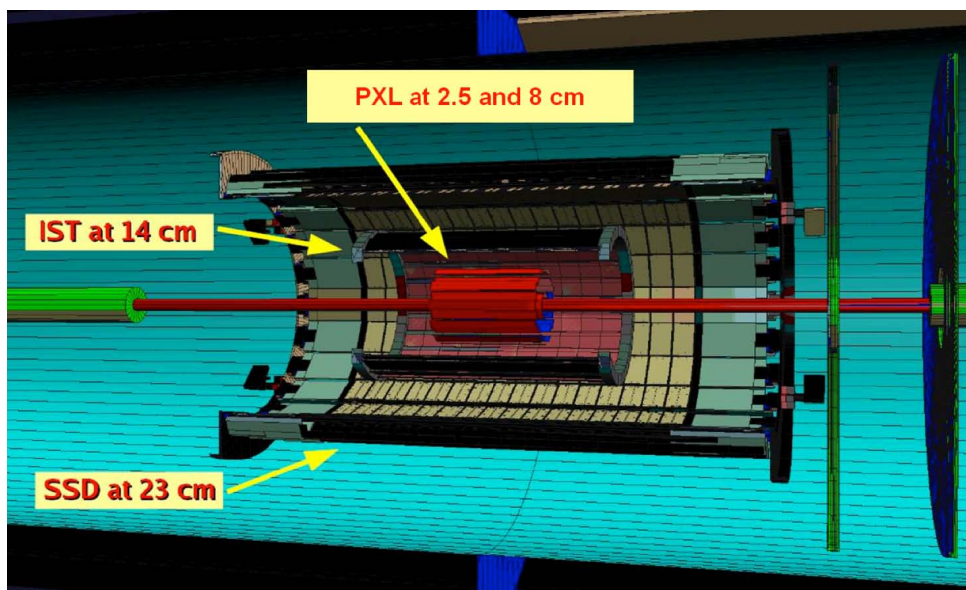


Figure 3.9: The Heavy Flavor Tracker. PXL - Pixel detector, IST - Intermediate Silicon Tracker, SSD - double-sided Silicon Strip Detector [17].

Both detectors, the SPD and the IST, lie inside the radial location of the Silicon Strip Detector. The IST is a strip detector designed to match the high resolution of the PIXEL detector with the high resolution of the TPC and the SSD. The IST consists of two layers. The inner layer lies at a radius of 12 cm and consists of 19 ladders of 40 cm length [28]. The outer layer lies at a radius of 17 cm and consists of 27 ladders of 52 cm length. The strips on the inner layer are oriented to give the

best resolution in the $r - \phi$ direction, while the strips of outer layer are oriented to give the best resolution in z direction.

The PIXEL detector is a low mass detector and it is located close to the beam pipe. It is also composed of two layers. The outer layer is located at a 7 cm radius and consists of 24 ladders. The inner one is located at a radius of 2.5 average radius and has 9 ladders. As the PIXEL is located as close as possible to the interaction point without residing inside the RHIC beam pipe, it achieves the maximum resolution.

Chapter 4

Algorithms of jet reconstruction

4.1 Introduction

The central concepts in the discussions of the QCD aspects of high energy collisions are quarks and gluons (or partons). As a result of the inability to observe partons, jets are measured instead. A jet is a narrow cone of hadrons and other particles produced by the hadronization of a quark or gluon in particle physics or heavy ion experiment (Figure 4.1). Jets are measured in particle detectors and studied in order to determine the properties of the original quarks. In heavy-ion physics jets play an important role as tomographical probes of the hot and dense matter/QGP.

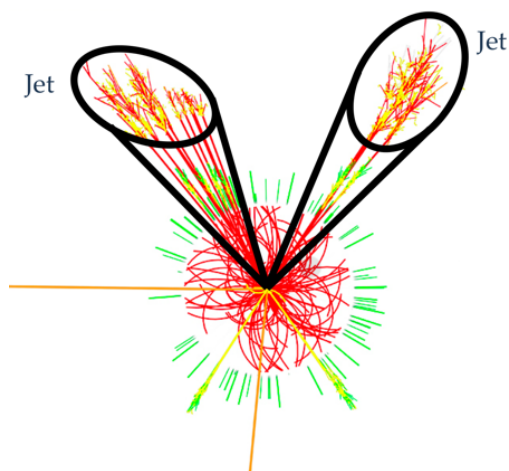


Figure 4.1: A schematic view of jets created in a heavy-ion collision [18].

There are two types of jets: regular or "soft-resilient" and less regular or "soft-adaptable". Having a regular jet can simplify some theoretical calculations as well as eliminate some parts of the momentum resolution loss caused by underlying event (UE) and pile-up contamination. Meanwhile, in the second type an infrared and collinear (IRC) safe algorithm can stimulate irregularities in the boundary of the final jet.

In order to reconstruct jets different algorithms are used. The jet finding algorithms can be divided into two types: cone jet-finders and sequential-clustering jet-finders.

The cone jet finding algorithms are based on identifying energy-flow into cones in pseudorapidity $\eta = -\ln \tan \frac{\theta}{2}$ and azimuth ϕ .

Cluster-type jet algorithms are based on successive pair-wise recombination of particles. They are infrared safe.

4.2 Attributes of the ideal jet algorithm

In order to treat the issues of the changing jet energy and angle definitions between the experiments and also to consider the phenomena of merging and splitting or role of the seed towers with the related soft gluon sensitivity the following four criteria were chosen:

1. *Full specification*: all parts of the algorithm, such as merging, splitting, etc., and all the algorithmic processes should be clearly and completely described.
2. *Theoretically well behaviour*: the algorithm should be IRC safe.
3. *Detector independence*: the algorithm should not depend on the cell type, numbers or size.
4. *Order independence*: the equality of the algorithm at the parton, particle and detector levels.

The first two criteria should be fulfilled by each algorithm. The last two should be approximately satisfied.

4.2.1 Theoretical attributes of the ideal jet algorithm

From the theoretical point of view the following characteristics are desirable for an "ideal" jet algorithm:

1. *Infrared and collinear safety*: the algorithm should not only be IRC safe, but should also find jets that are insensitive to any soft and collinear radiation in the event.

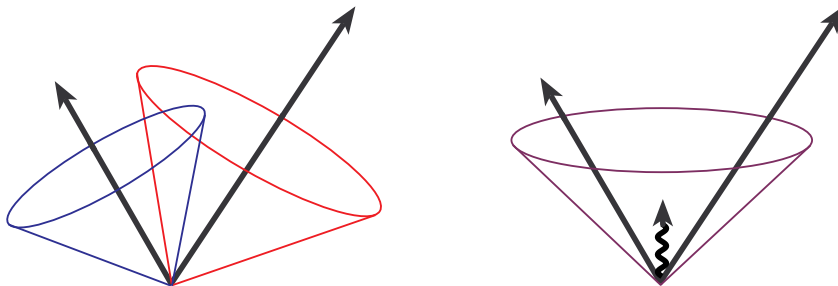


Figure 4.2: An example of infrared sensitivity in cone jet clustering [19].

As illustrated in Figure 4.2, jet clustering begins around seed particles that are shown as arrows with the length proportional to energy.

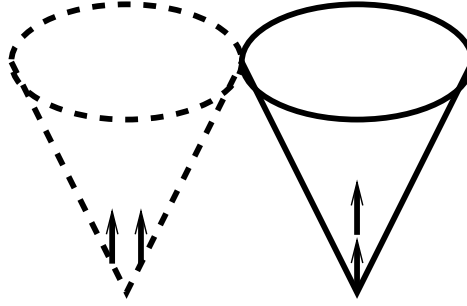


Figure 4.3: Collinear sensitivity in jet reconstruction [19].

Figure 4.3 illustrates the collinear sensitivity in jet reconstruction. As it can be seen the left cone cannot produce a seed because of the splitting energy among several detector towers, while the right cone produces a seed due to the more narrowly distributed energy.

2. *Invariance under boosts*: in proton-proton collisions it is especially important to find the same solutions which are independent of boosts in the lengthwise direction.
3. *Boundary stability*: the kinematic variables used to describe the jets should preferably exhibit kinematic boundaries that are insensitive to the details of the final state. It is important to have boundary stability in order to perform soft gluon summations.
4. *Order independence*: the same jets should be found at the parton, particle and detector level.
5. *Straightforward implementation*: it is desirable for the algorithm to be easy to implement in perturbative calculations.

4.2.2 Experimental attributes of the ideal jet algorithm

After jets enter a detector, different effects, such as particle showering, noise, detector response, etc., will to some extent influence the performance of even the most ideal jet algorithm. In order to minimize the amount of corrections in algorithm the following criteria were added:

1. *Detector independence*: the algorithm should be as independent as possible on the detector that provides the data.
2. *Minimization of resolution smearing and angle biases*: the unavoidable effects should not be amplified of resolution smearing and angle biases by the algorithm.
3. *Stability with luminosity*: multiple hard scatterings at high beam luminosities should not affect the jet finding. In addition, there should be no dependence of the algorithm on the jet angular and energy resolutions.

4. *Efficient use of computer resources:* the jet algorithm should provide jet identification with a minimum of computer time. Inasmuch as changes in algorithm intended to minimize the necessary computer time can lead to problems in the comparison with theory, it is better to invest in more computer resources.
5. *Maximal reconstruction efficiency:* all physically interesting jets should be efficiently identified.
6. *Ease of calibration:* the absence of obstacles to the reliable calibration of the kinematic jet's properties is desirable for the algorithm.
7. *Ease of use:* it is desirable for the algorithm to be easy to implement with typical experimental detectors and data.
8. *Full specification:* clustering, energy and angle definition, and all details of jet splitting and merging should be fully specified for each algorithm.

4.3 Cone jet finding algorithms

Cone algorithms are the first algorithms that were used for jet finding. Initially, cone jet-finders were used only for the hadron-hadron experiments. The main idea of these algorithms is following. A cone with the radius R consists of all the particles whose trajectories lie inside the area $A = \pi R^2$ in $\eta \times \phi$ space. Further, the axis of the cone should coincide with the jet direction. In order to minimize computing time an iterative process of a stable cone choosing starts only with the cones which have the most energetic particle ("seed") in its center. These seeds are also required to pass a threshold energy of few hundreds MeV.

E_T -weighted centroids are calculated for the particles in each seed cone. Then these centroids can be used as centers for new cones in $\eta \times \phi$ space. The process repeats until the cone axis coincides with the centroid. However, one particle can belong to two or more cones thereby leading to their overlapping. That means that a procedure should be included in the jet algorithm to specify how to merge or split such overlapping cones.

Unfortunately, the cone algorithms were not so effective. Also they infringe the IRC safety. Thus, in my thesis we will focus not on the cone jet-finders, but on the cluster-type jet algorithms that are described in more detail below.

4.4 Cluster type jet finding algorithms

The wide usage of sequential-clustering jet algorithms at different accelerators, such as Tevatron in Fermilab and the LHC at CERN, led to intense discussions concerning the advantages of various types of jet algorithms. One part of the discussion has concentrated on the merits of sequential recombination (kT and Cambridge/Aachen) and cone algorithms, another has centered on the anti-kT jet-finder. The difference between the kT and cone methods is in their sensitivity to non-perturbative effects like hadronization and underlying event (UE) contamination.

Two types of distances are defined in cluster jet-finding algorithms. The first is the distance d_{ij} between entities i and j . The second one is the distance d_{iB} between the particle i and the beam B . These distances are defined as follows

$$d_{ij} = \min(k_{ti}^{2p}, k_{tj}^{2p}) \frac{\Delta_{ij}^2}{R^2}, \quad (4.1)$$

$$d_{iB} = k_{ti}^{2p}, \quad (4.2)$$

where $\Delta_{ij}^2 = (y_i - y_j)^2 + (\phi_i - \phi_j)^2$ and k_{ti} , y_i , ϕ_i and R are the transverse momentum, rapidity, azimuth and radius parameter of particle i respectively. A parameter p is used to take control of the relative power of the energy versus geometrical (Δ_{ij}) scales.

The clustering jet algorithm identifies d_{min} , the smallest of the distances, and if it is d_{ij} then it recombines the entities i and j , otherwise, if the smallest distance is d_{iB} , it calls i a jet and removes it from the list. The procedure is repeated until no particles are left.

Depending on the value of the parameter p the algorithms are divided into three types: kT, anti-kT and Cambridge/Aachen algorithms. Hereafter, the first two algorithms will be described in more detail.

4.4.1 kT algorithm

For this type of the jet finding algorithm $p = 1$. After finding the minimum distance d_{min} between all the d_{ij} (Eq. 4.1) and d_{iB} (Eq. 4.2) there could be two situations: $d_{min} = d_{ij}$ or $d_{min} = d_{iB}$.

- In the first case, the particles i and j are merged, summing their four-momenta.
- In the second one, a particle is declared to be a final jet and next is removed from the list.

This algorithm has its advantages and disadvantages. The first advantage is the explicit imitation of a walk through the QCD branching sequence. This means, that the largest part of the particles radiated from an original hard parton is clustered in the reconstructed jets. That gives better particle mass measurements, general kinematic reconstruction and gaps-between-jets identification. The second advantage of the kT algorithm is jet disintegration into constituent subjets. That is useful for identifying decay products of fast-moving heavy particles. The main disadvantage of the kT jet-finder is its algorithmic slowness: clustering N particles into jets requires $\mathcal{O}(N^3)$ operations. For instance, the cluster time would grow to an unsustainable $\mathcal{O}(10^5 s)$, i.e. more than a day, for a typical heavy-ion event at the LHC, $N = \mathcal{O}(50000)$. That is why the kT jet-finder slowness had been initially one of the instigating factors behind proposals for alternative algorithms. Now this problem has been already solved (will be described in Section 4.5) [21]. Because of the the jet-finder's sensitivity to a background in comparison with the other algorithms it is mostly used for the background estimation.

4.4.2 Anti-kT algorithm

For this type of the jet finding algorithm the parameter $p = -1$. The behaviour of the anti-kT algorithm can be explained on the event containing a few well-separated hard particles with transverse momenta k_1, k_2, \dots and many soft particles. In contrast to the kT jet-finder, the hardest particle is found first and after that the algorithm searches for the distances between this hard particle "1" and soft particles. These distances are defined only by the hard particle's transverse momentum and the Δ_{1i} separation. The shape of the final jet depends on the distance between the two hard particles.

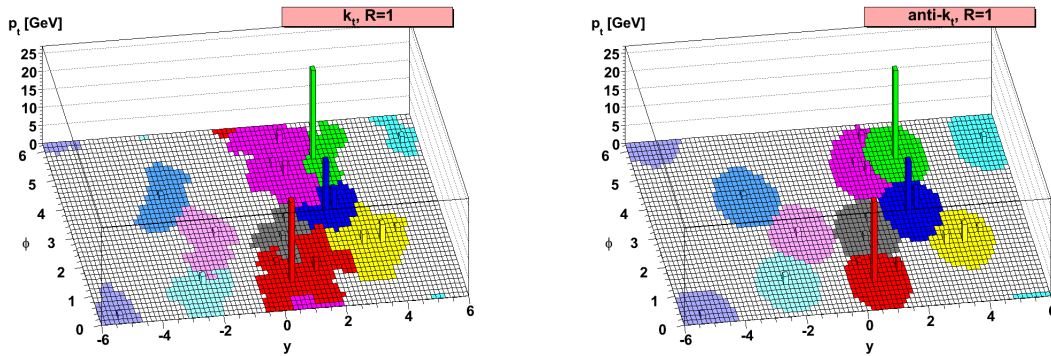


Figure 4.4: A sample parton-level event generated with HERWIG Monte-Carlo generator of p+p collision clustered with kT and anti-kT algorithms [20].

- In case there are no other hard particles within a distance of $2R$ from the given hard particle, the hard particle that does not have any other hard particles around itself within a distance of $2R$ from it will easily collect all the soft particles within a circle radius R . The result will be a perfect conical jet.
- In case the second hard particle is situated within a distance $R < \Delta_{12} < 2R$, there will be two hard jets. There is no possibility of having two perfect conical jets at the same time. Thus, there are three cases: $k_{t1} \gg k_{t2}$, $k_{t1} = k_{t2}$ and $k_{t1} \sim k_{t2}$.
 - If $k_{t1} \gg k_{t2}$, the first jet will have a conical shape and the second jet will be partly conical since it will miss the part crossing the first jet.
 - If $k_{t1} = k_{t2}$, neither of two jets will be conical and the overlying area will be easily divided by a straight line into the two equal parts.
 - In general state, when $k_{t1} \sim k_{t2}$, a boundary b defined as $\Delta R_{1b}/k_{t1} = \Delta_{2b}/k_{t2}$ will be pruned both of cones.
- In case $\Delta_{12} < R$ two particles will cluster to form a single jet.
 - If $k_{t1} \gg k_{t2}$, it will be a conical jet centered around k_1 .
 - If $k_{t1} \sim k_{t2}$, it will be the union of cones with radius $< R$ around each hard particle plus one cone with radius R centered on the final jet.

Figure 4.4 shows the behaviour of the k_T and anti- k_T algorithms. A parton-level event was taken together with $\sim 10^4$ random ghost particles and then clustered with four different algorithms. It can be seen that the pair of jets near $y = 2$ and $\phi = 5$ presents an interesting example in the respect of jet shapes. The left-handed one is much softer than the right-hand one. Also the k_T jets have an irregular boundary between jets, while the anti- k_T algorithm has circular generated hard jet, which trims a lens-shaped region out of the soft one, leaving behind a crescent.

Area related properties

In order to discuss the properties of jet boundaries for different algorithms, the calculations of jet areas are used. There are two types of jet areas: passive and active. The first type measures jet's susceptibility to point-like radiation. The second one measures its susceptibility to diffuse radiation.

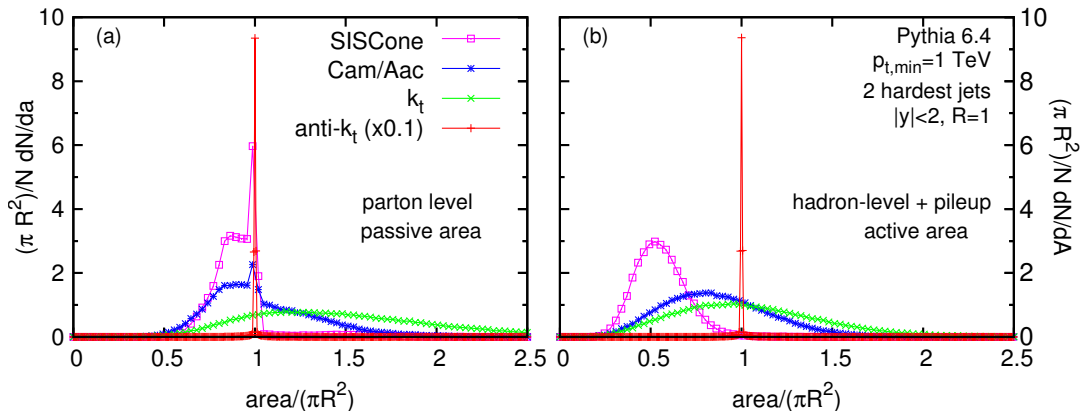


Figure 4.5: Distribution of areas in di-jet events at the LHC for various jet finding algorithms (see legend). (a) passive area at parton level, (b) active area at hadron level including UE and pile-up [20].

The passive area $a_{JA,R}(\Delta_{12})$ in usual IRC safe jet algorithms is πR^2 only when $\Delta_{12} = 0$, but when Δ_{12} is increased, it changes. For comparison, the passive area of anti- k_T jets is always independent of Δ_{12} : $a_{anti-kT,R}(\Delta_{12}) = \pi R^2$, since its boundaries are unaffected by soft radiation. For the anti- k_T algorithm also applies that the passive and active areas are identical.

The distribution of areas in di-jet event at the LHC energy generated by PYTHIA 6.4 Monte-Carlo event generator is illustrated in the Figure 4.5. In the left panel the passive area of the anti- k_T algorithm is compared with those for other algorithms (SIScone, Cambridge-Aachen, k_T). Similar comparison is shown for the active area in Figure 4.5b.

Figure 4.6 shows the average area in di-jet events at the LHC generated by Monte-Carlo generator HERWIG 6.5. The yellow band around the anti- k_T algorithm coincides with the area fluctuations.

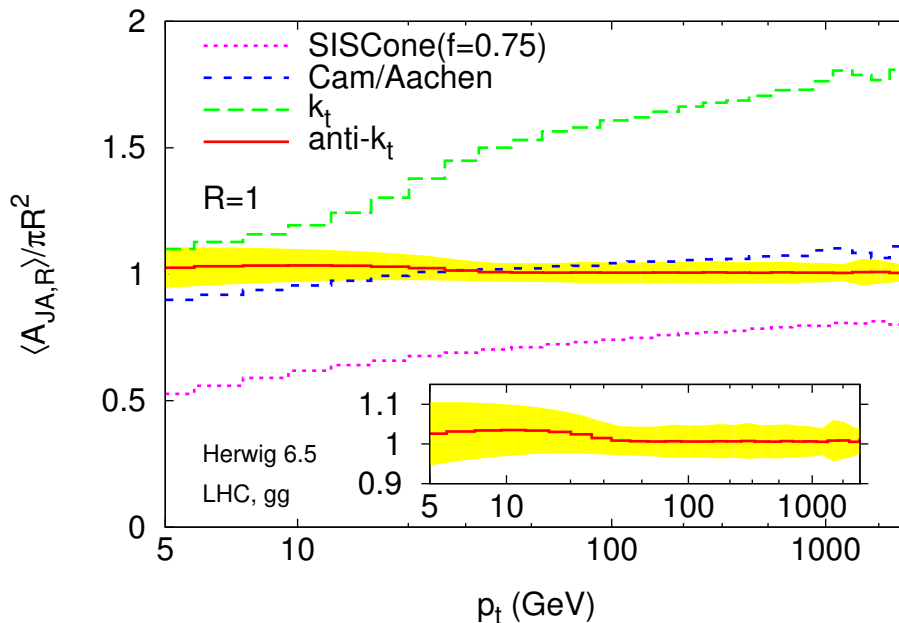


Figure 4.6: The mean area in di-jet events at the LHC for various jet finding algorithms (see legend) [20].

Back reaction

Suppose one has a hard scattering event that leads to a set of jets $\{J_i\}$. After adding a soft event (UE, pile up) and rerunning the algorithm one gets a set of jets $\{\tilde{J}_i\}$ that differ in two ways. First of all, the soft energy will be added to each jet. Secondly, there could be a change of the distribution of the particles from the hard event: in case a \tilde{J}_i that is close to the original J_1 will be found, then two jets will not consist from the same subset of particles from the original hard event. This is called "back reaction".

It can be shown for the anti- k_T algorithm that the back reaction probability is suppressed not by the amount of back reaction itself, but by the transverse momentum of the jet, p_t , that leads to a much smaller effect. This makes the anti- k_T algorithm the most suitable in the environment with the big background which is in heavy-ion collisions.

4.5 FastJet

FastJet is a software package [29], [21], [20] where most of jet finding algorithms are implemented. This package also includes tools for calculating jet areas and performing background (pile-up/UE) subtraction and for jet substructure analyses. An interested reader can find more information in these [30], [31] articles.

Identifying each particles geometrical nearest neighbour with a help of a Voronoi diagram and a Delaunay triangulation it isolates the geometrical aspects of the problem. Due to this, the FastJet requires only $\mathcal{O}(N \ln N)$ operations versus the k_T jet-finder. Figure 4.7 compares the running time of the FastJet with the k_T jet-finder.

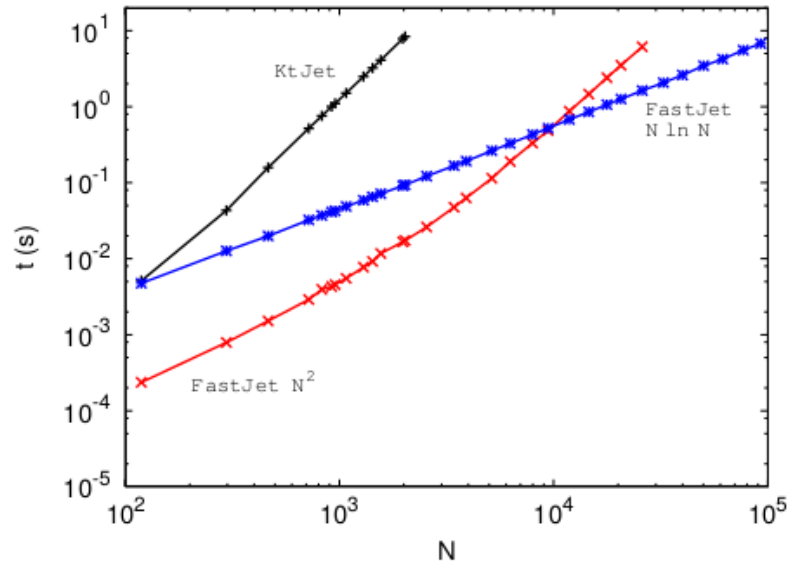


Figure 4.7: The running times of kT jet-finder and FastJet implementations of the kT clustering algorithm versus the number of initial particles [21].

The reduction of the kT algorithm complexity from N^3 to $N \ln N$ operations opens up the previously unconvincing usage of the kT jet-finder for the large values of N that rise when considering all cells of a finely segmented calorimeter and for heavy-ion events.

Chapter 5

JEWEL

5.1 Introduction

JEWEL [22], [23] is a Monte Carlo event generator for jets in heavy ion collisions. Only jets are simulated in JEWEL. That implies that the UE in p-p and the remaining event in nucleus-nucleus collisions are not included.

JEWEL is based on a perturbative language for jet's evolution and interaction description in a medium (in a common framework). If the objects cannot be described in a perturbative language, hard scatterings of composite objects, e.g. protons, can still resolve the partonic structure of interacting objects because the non-perturbative structure has no influence on hard interactions. The same hypothesis was applied to hard interactions of a jet in QGP. That means that standard perturbative techniques can describe such hard interactions. The following assumptions underlie the JEWEL construction:

- The medium that is resolved by the jet consists of a collection of quasi-free partons.
- An infrared continuation of the perturbative matrix elements can be used to include the main effect of soft scattering.
- The formation times of the emissions determine the interaction between competing radiative processes.
- The physical picture behind the LPM effect received in the eikonal limit is valid also in general kinematics.

The fact that a fully microscopic description of jet interpretation in a medium including coherence effects is implemented in JEWEL leads to its complexity.

5.2 Physics of JEWEL

The matrix elements at fixed order in perturbation theory are used in QCD to describe hard scattering process. Further, only the lowest order scattering processes (three level $2 \rightarrow 2$ processes) will be considered. Insomuch as radiative corrections can be large, they need to be taken into account. The main contribution of radiative corrections has a simple structure and does not rely on the type of hard scattering

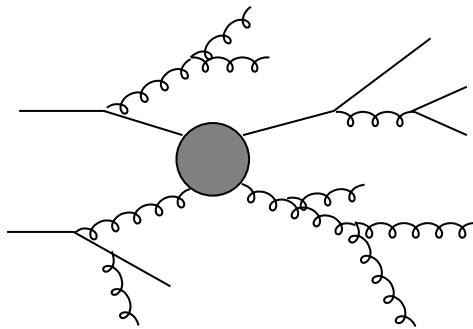


Figure 5.1: Schematic picture of extra emissions generated by the parton shower on top of a hard quark-gluon scattering effect described by a $2 \rightarrow 2$ matrix element [22].

under consideration. Due to this, the approximations to the full higher order matrix elements can be systematically constructed. In order to accomplish this in Monte Carlo event generators, it is first needed to generate a hard scattering configuration from the $2 \rightarrow 2$ matrix elements and then add the leading radiative corrections with a parton shower. The latter one thus attaches extra emissions to all incoming and outgoing legs on the hard scattering, as demonstrated in Figure 5.1.

The parton shower does not affect the cross section, but generates any number of extra emissions, which are ordered in a variable characterizing their hardness (i.e. the transverse momentum of the emission or the virtuality). In the initial state the hardness rises until the scale of the matrix is reached, while in the final state it diminishes. As in the IR region the probability for gluon emission diverges, the parton shower has to be cut off at a suitable scale.

The proton PDFs¹ restrain the protons shower action in the initial state because of the proton structure formation at different scales by the emitted partons. The PDFs also help the initial state parton shower to know that the partons originate from a hadron of a certain structure. In the hard re-scattering of a hard parton off a constituent of a strongly interacting medium the incoming partons are not a part of a proton. This fact differs the hard re-scattering from the hard partonic scattering in a p-p collision.

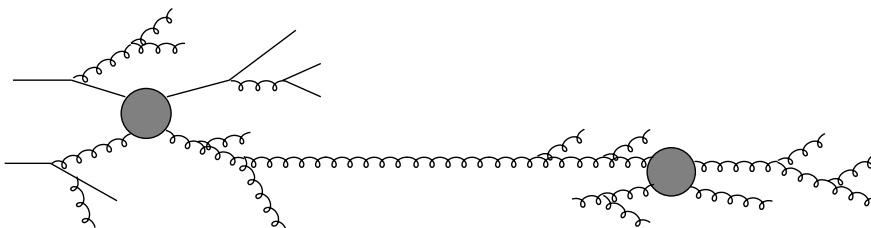


Figure 5.2: Schematic picture of extra emissions in two well separated events. The re-scattering is only indicated for one parton [22].

¹The **P**arton **D**istribution **F**unction is the distribution function defined as the probability density for finding a particle with a certain longitudinal momentum fraction x at resolution scale Q^2 , where Q^2 is the energy scale of the hard interaction. The precise knowledge of proton PDF is essential for making predictions for the Standard Model and beyond the Standard Model processes at hadron colliders [32].

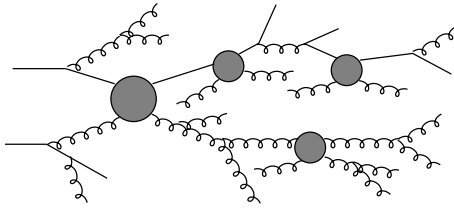


Figure 5.3: Schematic picture of extra emissions and re-scatters taking place on comparable time scales [22].

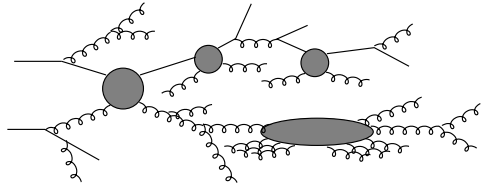


Figure 5.4: Schematic picture of extra radiation and re-scattering where several momentum transfers can act coherently to induce an emission [22].

The complication in using the matrix elements and parton showers to describe the perturbatively hard re-scattering of a parton in a medium is that there is no natural IR cut-off. p - p collisions usually guarantee the matrix element to be sufficiently hard because of the requirements of analysis. Thus for instance, in jet production the jets will be required to have a certain p_{\perp} . In the re-scattering in the medium very soft momentum transfers will not lead to any visible effects. Therefore, the second assumption is used.

It was assumed that the distance between the initial jet production and the first re-scattering is large in comparison to the time for the parton shower evolution (Figure 5.2).

Nevertheless, it should not be true inasmuch as the initial jet production happens in the same nuclear collisions as the formation of the medium and the radiation during parton shower evolution happens with a certain formation time. In case of two emissions taking place at the same time the emission with a shorter formation time gets formed as an individual parton at the end of its time while the other one is rejected. That situation is sketched in Figure 5.3.

When the formation times overlap the radiation induced by subsequent scatterings interferes destructively because of the analytical calculations of Bremsstrahlung induced by multiple scattering (LPM effect). Using an iterative algorithm to establish the formation time of the emission and the coherently contributing momentum transfers the LPM effect can be considered in a probabilistic formulation. According to the fourth assumption the probabilistic algorithm can still be used. That implies that in some cases the effective momentum transfer (Figure 5.4) and emissions have to be rejected with a certain probability.

Insomuch as JEWEL makes no assumptions about the nature of the medium, it requires to be provided with the phase space density of scattering centres.

5.3 A simple model of the medium

In order to understand which features in the data can be accounted for by microscopic dynamics it is good to work with a simple model of the medium. It is assumed that initial di-jet production takes place at $t = z = 0$, where z is the beam direction.

The initial temperature T_i in the centre ($x=y=0$) of a central collision ($b=0$) and the proper time τ_i at which the evolution starts determine the initial conditions for the hydrodynamic evolution. For simplicity a symmetric A+A collision is assumed.

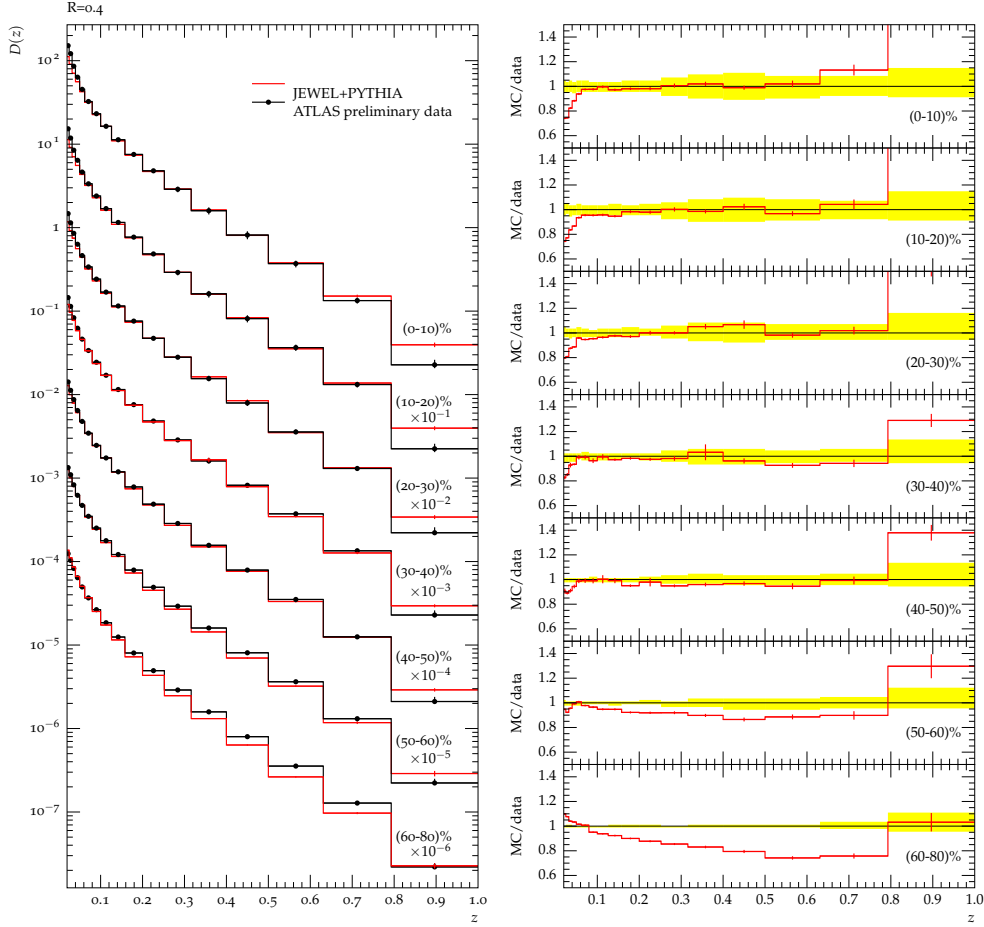


Figure 5.5: Centrality dependence of the intra-jet fragmentation function $D(z)$ in Pb+Pb collisions at $\sqrt{s_{NN}} = 2.76$ TeV for a jet radius $R = 0.4$, $p_{T,jet} > 100$ GeV/c and $\eta_{jet} < 2.1$ [23].

The initial energy density $\epsilon(b; x, y, \tau_i)$ is proportional to the density of participants

$$\epsilon(b; x, y, \tau_i) = \epsilon_i \frac{n_{part}(b; x, y)}{\langle n_{part} \rangle (b=0)} \quad \text{with} \quad \langle n_{part} \rangle (b=0) \approx \frac{2A}{\pi R_A}, \quad (5.1)$$

and consequently, the transverse profile is fixed. In the Eq. 5.1 R_A is the radius of the nucleus and $\epsilon_i \propto T_i^4$ is related to the initial temperature.

The hydrodynamic evolution presumes Bjorken expansion neglecting transverse expansion and an ideal gas equation of state:

$$\epsilon(b; x, y, \tau) = \epsilon(b; x, y, \tau_i) \left(\frac{\tau}{\tau_i} \right)^{-\frac{4}{3}}, \quad (5.2)$$

$$T(b; x, y, \tau) \propto \epsilon^{1/4}(b; x, y, \tau_i) \left(\frac{\tau}{\tau_i} \right)^{-\frac{1}{3}}. \quad (5.3)$$

Here, τ_i is the initial time of the hydrodynamic evolution. It is assumed that the temperature increases linearly with τ for proper times earlier than τ_i . Characterization of the jet evolution by the high scales set by the initial jet production such

that it is protected from disturbances due to re-scattering in the medium results in a very little sensitivity of JEWEL to the assumptions about the very early phase of the medium. Notwithstanding this simple model reflects important characteristics, e.g. the rapid longitudinal expansion, of heavy ion collisions, it nonetheless misses certain other aspects, most importantly the transverse expansion.

Figure 5.5 shows an example of using JEWEL in practice. Here, the intra-jet fragmentation function $D(z)$ measured by the ATLAS Collaboration in Pb-Pb collisions at $\sqrt{s_{NN}} = 2.76$ TeV at the CERN LHC as a function of collision centrality is depicted. In general, there is a reasonable agreement between data and JEWEL simulations as can be seen from the right panel of the Figure 5.5, where the ratio of MC/data is plotted. Even in the last two centrality classes the JEWEL+PYTHIA results are below the ATLAS data with the largest deviation about 25%.

Chapter 6

Analysis of jets

6.1 Jet shapes

In order to understand the mechanisms of energy loss of partons in the medium and the properties of the medium itself, one should measure the modifications of the jet yield and fragmentation relative to p-p collisions. For this aim different jet shape observables are used.

The first is the *radial moment* g , which measures the radial energy profile of the jet. The radial moment is given by the equation:

$$g = \sum_{i \in \text{jet}} \frac{p_{T,i}^i}{p_{T,\text{jet}}} |\Delta R_{i,\text{jet}}| \quad (6.1)$$

where $p_{T,i}^i$ stands for the momentum of constituent i and $\Delta R_{i,\text{jet}}$ is the distance in $\eta \times \phi$ plane between constituent i and the jet axis [33]. This shape is sensitive to the collimation or broadening of the jet.

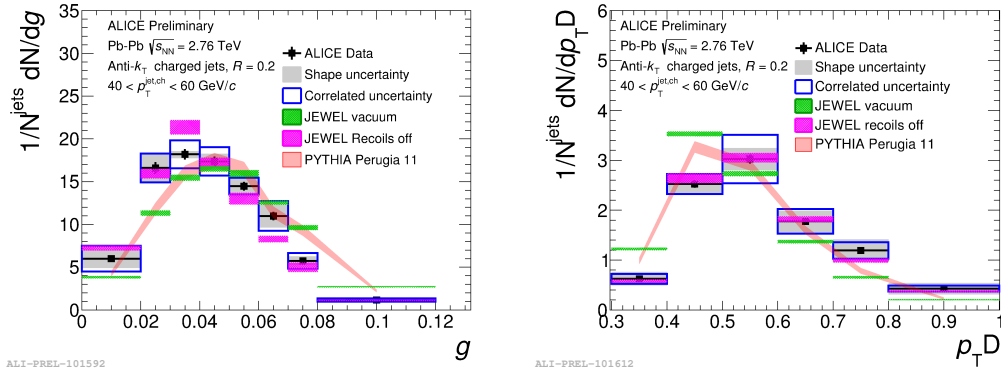


Figure 6.1: Fully corrected g (left) and $p_T D$ (right) distributions for the jet resolution parameter $R = 0.2$ in Pb-Pb collisions at $\sqrt{s_{NN}} = 2.76$ TeV at ALICE compared to PYTHIA Perugia 11 and JEWEL models [24].

The next jet shape observable is the *momentum dispersion* $p_T D$, which measures the second moment of the constituent p_T distribution in the jet and provides the information about hardness/softness of the fragmentation. In case of large number

of constituents the $p_T D \rightarrow 0$, while in the opposite situation, i.e. the small number of constituents, the $p_T D \rightarrow 1$. The momentum dispersion is defined as follows:

$$p_T D = \frac{\sqrt{\sum_{i \in jet} p_{T,i}^2}}{\sum_{i \in jet} p_{T,i}}. \quad (6.2)$$

Figure 6.1 shows the fully corrected shape distributions in Pb-Pb collisions at $\sqrt{s_{NN}} = 2.76$ TeV at ALICE compared to PYTHIA Perugia 11 in the same jet p_T range of 40-60 GeV/c. As it can be seen, the radial moment is shifted to lower values (left plot) while the momentum dispersion is shifted to higher values (right plot) in data compared to PYTHIA. That means, that the jet cores in Pb-Pb collisions are harder than the jet cores in PYTHIA at the same energy.

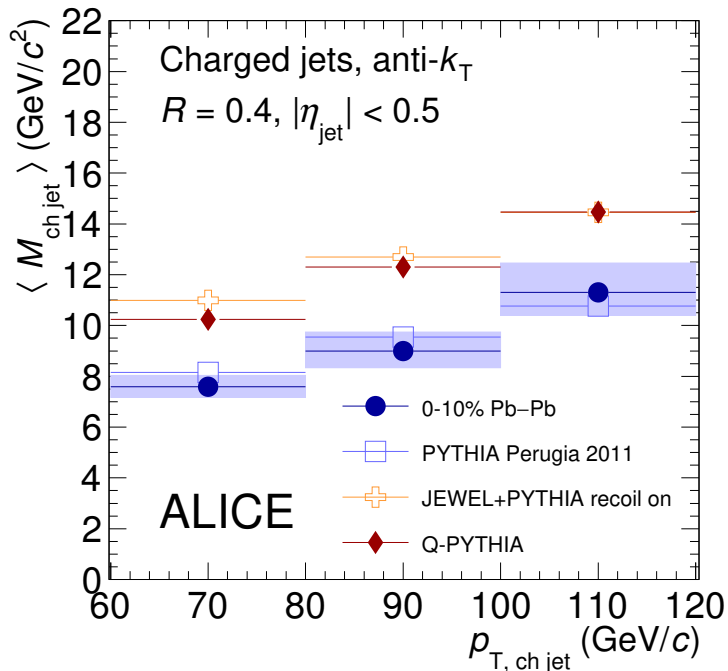


Figure 6.2: Fully-corrected mean jet mass compared to PYTHIA Perugia 2011 and the jet quenching event generators (JEWEL and Q-PYTHIA) for anti-kt jets with $R = 0.4$ in the 10% most central Pb-Pb collisions [25].

The third jet shape observable is the *jet mass* [25]. This shape increases once the parton fragmented due to the rise of the high- p_T parton virtuality after its subsequent interactions with other partons of the medium. The jet mass can be calculated from the jet four-momentum as follows:

$$M_{jet} = \sqrt{E_{jet}^2 - p_{T,jet}^2 - p_{z,jet}^2}, \quad (6.3)$$

where E_{jet} is the jet energy and $p_{z,jet}$ is its longitudinal momentum.

Figure 6.2 compares mean jet mass as a function of $p_{T,ch,jet}$ measured in the Pb-Pb collisions at $\sqrt{s_{NN}} = 2.76$ TeV at ALICE to PYTHIA Perugia 2011 and jet

quenching generators. As it can be seen, the vacuum expectation from PYTHIA is compatible with the Pb–Pb measurement within systematic uncertainties, while the JEWEL+PYTHIA "recoil on" and Q-PYTHIA significantly overestimates the jet mass.

There are other jet shape observables, but in this thesis we will focus on the radial moment (Eq. 6.1) and the momentum dispersion (Eq. 6.2).

6.2 JEWEL simulation

Below the JEWEL simulation on particle level will be presented. For this thesis we have simulated 500 thousands events for the vacuum model and 500 thousands events medium model using the parameters mentioned in the Tables (6.2) and (6.1) respectively. The charged particles were simulated in pseudorapidity $\eta_{cent} = 2.5$ and full azimuth. The resolution parameter R was chosen to be $R = 0.2$ and $R = 0.4$. All charged constituents were required to have $p_T \sim 200$ MeV. For jet reconstruction the anti-kT algorithm included in FastJet [29] software was used.

Name of parameter	Value
N protons	79
MASS	197
SQRTS, [GeV]	200
PTMIN, [GeV]	3
PTMAX, [GeV]	-1
ETAMAX	2.5

Table 6.1: Parameters for JEWEL simulation without medium. Here, MASS is the mass number of Au nucleus, N protons is the number of protons in Au nucleus, SQRTS is the CMS energy of the colliding system, PTMIN/PTMAX is the minimum/maximum p_T in matrix element, ETAMAX is the rapidity range $[-\text{ETAMAX}; \text{ETAMAX}]$ [22].

Name of parameter	Value
TI, [GeV]	0.28
TAUI, [fm]	0.6
A	197
CENTRMIN, [%]	0
CENTRMAX, [%]	10
SIGMANN, [fm ²]	4.2

Table 6.2: Parameters for JEWEL simulation with medium. TI is (mean) initial temperature, TAUI is the initial time τ_i , A is an integer mass number if colliding nuclei, CENTRMIN/CENTRMAX is the lower/upper end of centrality range to be simulated and SIGMANN is the nucleon-nucleon cross-section [22].

6.2.1 Results for the simulation with medium

The p_T spectra of charged jets with the resolution parameters $R = 0.2$ and $R = 0.4$ are depicted in Figure 6.3.

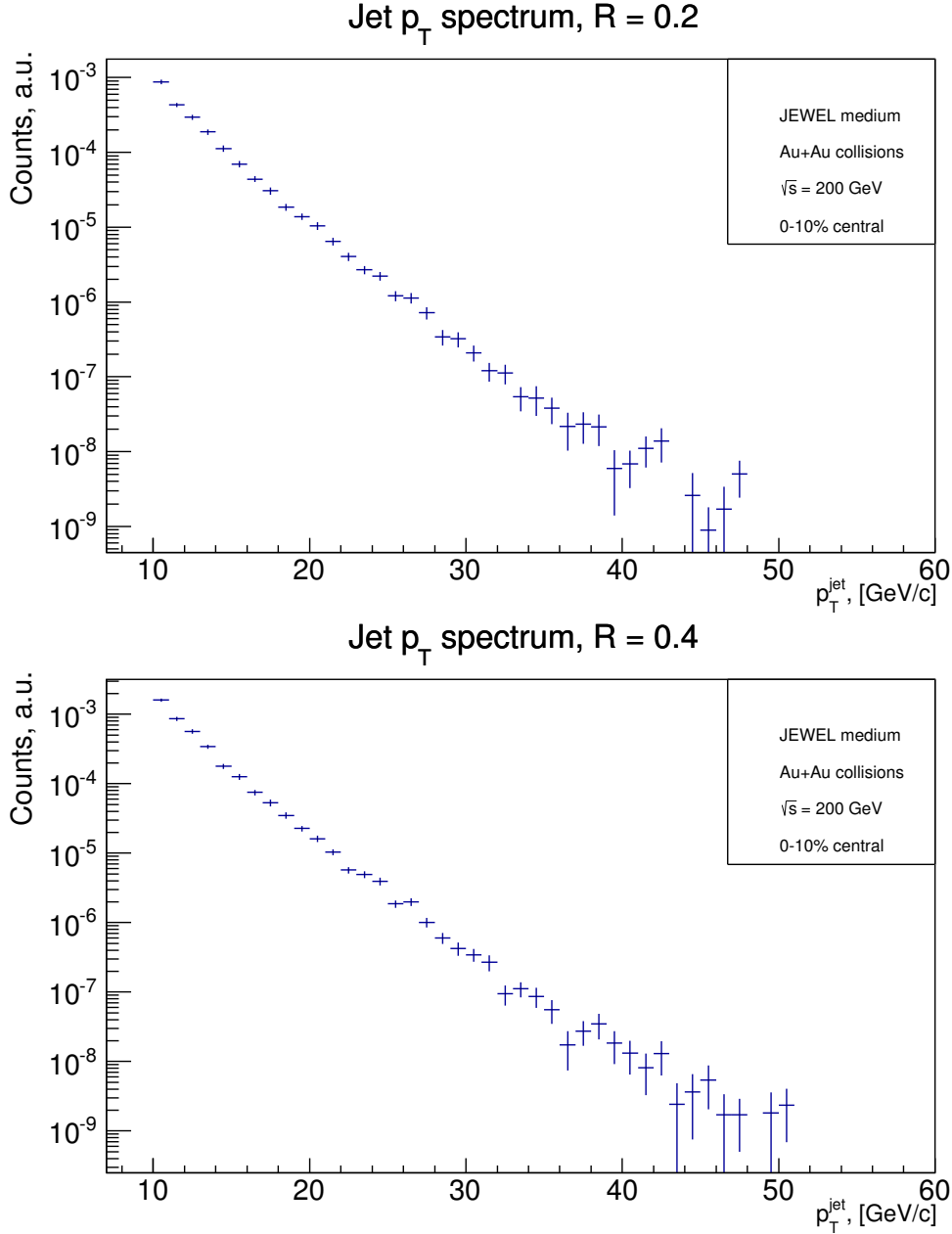


Figure 6.3: The p_T spectrum of charged jets for resolution parameter $R = 0.2$ (upper one) and $R = 0.4$ (lower one) of data simulated with medium.

As it can be seen, the p_T spectra have the exponential shape. All the jets have the $p_T > 10$ GeV/ c . For $R = 0.2$ the p_T spectrum is steeper than for $R = 0.4$.

Figure 6.4 shows the radial moment distributions of data simulated with medium with the resolution parameter $R = 0.2$. The simulation results are performed in two

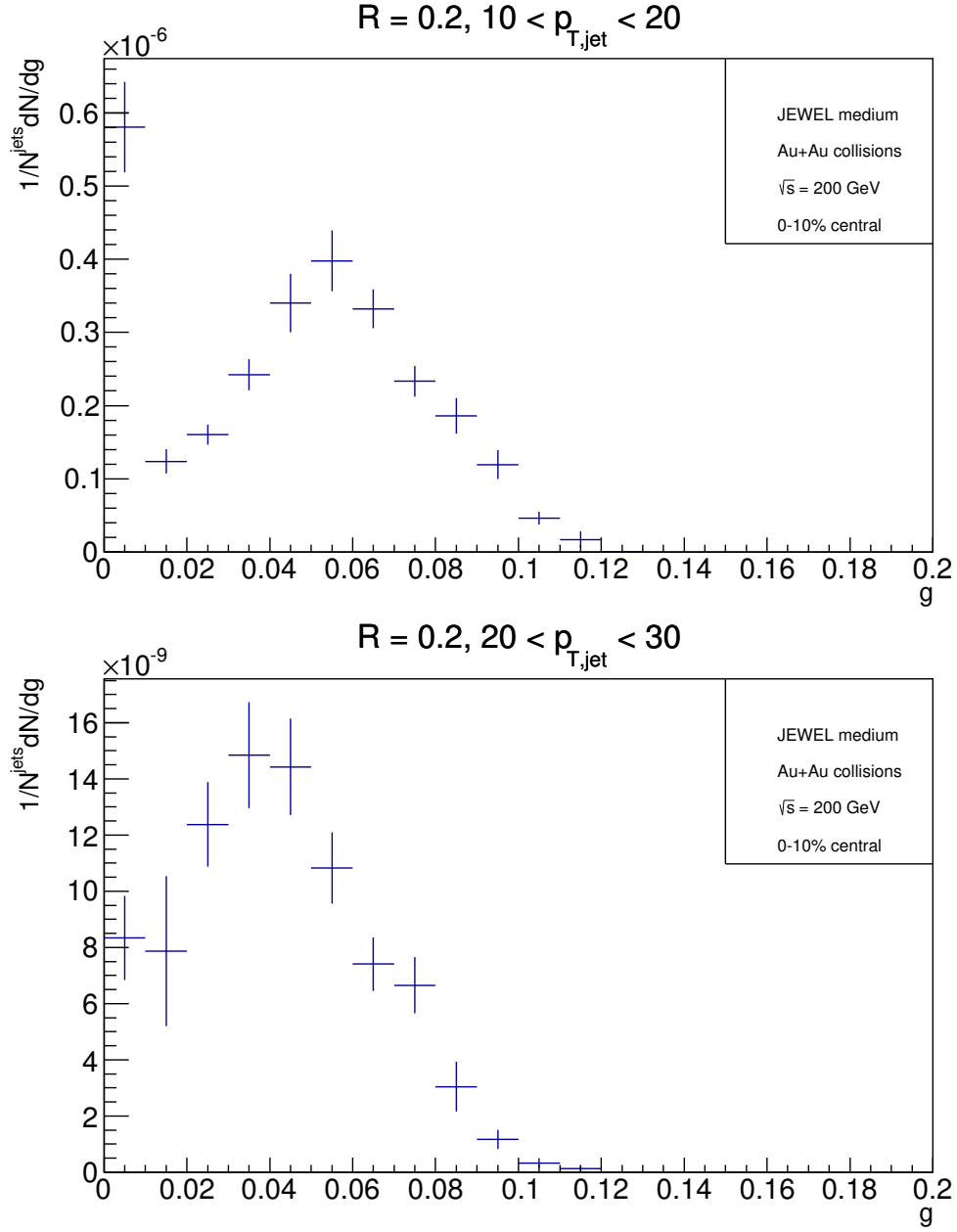


Figure 6.4: The radial moment distributions of data simulated with the resolution parameter $R = 0.2$ for two $p_{T,jet} \in < 10; 20 >$ GeV/c (upper one) and $p_{T,jet} \in < 20; 30 >$ GeV/c (lower one).

intervals of jet transverse momentum: $10 < p_{T,jet} < 20$ GeV/c (upper one) and $20 < p_{T,jet} < 30$ GeV/c (lower one).

Figure 6.5 shows the radial moment distributions of data simulated with medium with the resolution parameter $R = 0.4$. The simulation results are performed in two intervals of jet transverse momentum: $p_{T,jet} \in < 10; 20 >$ GeV/c (upper plot) and $p_{T,jet} \in < 20; 30 >$ GeV/c (lower plot).

As can be seen from the Figure 6.4 and Figure 6.5, there are points for $g < 0.01$,

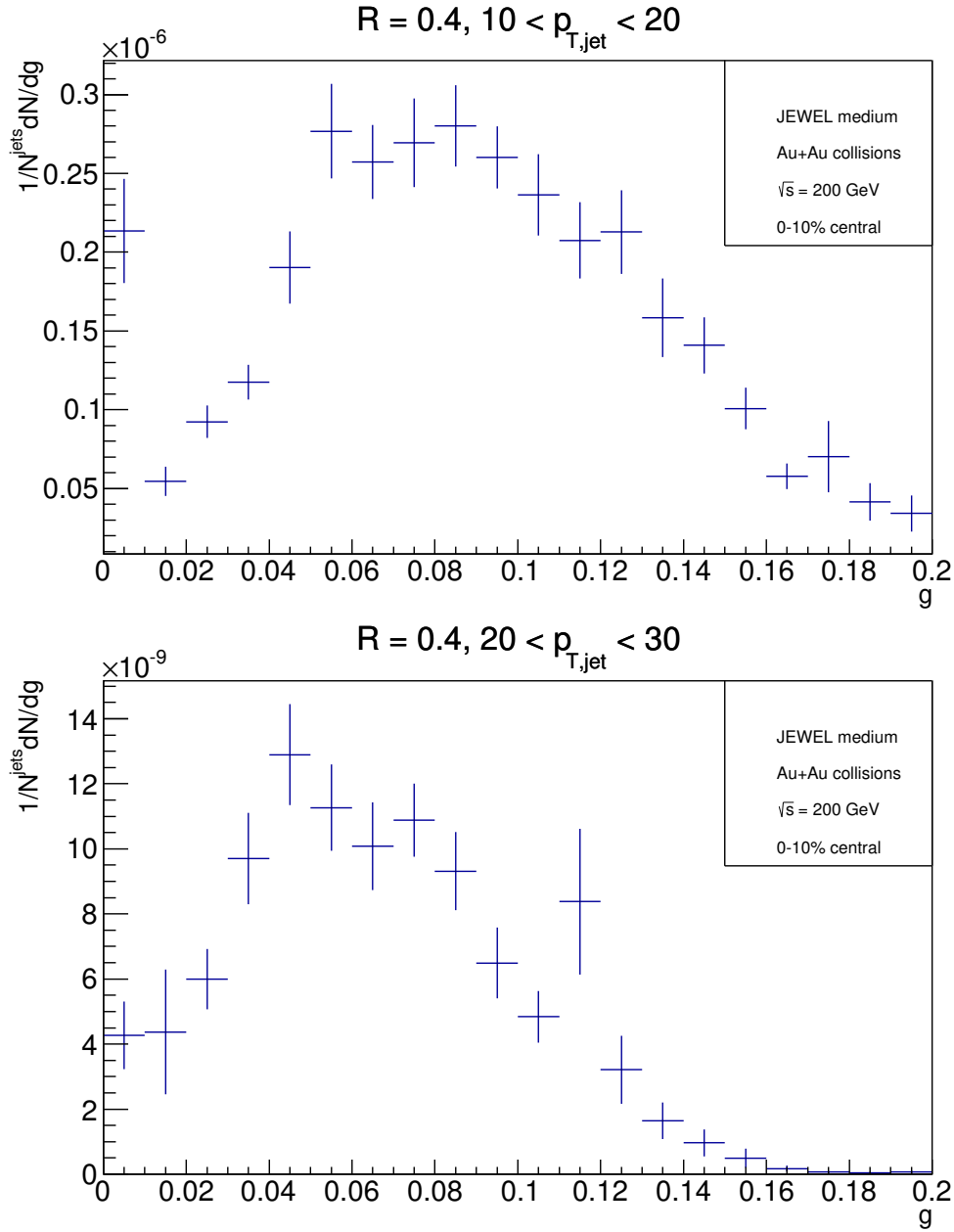


Figure 6.5: The radial moment distributions of data simulated with the resolution parameter $R = 0.4$ for two $p_{T,jet}$ intervals: $p_{T,jet} \in < 10; 20 > \text{GeV}/c$ (upper one) and $p_{T,jet} \in < 20; 30 > \text{GeV}/c$ (lower one).

which are located higher for the transverse momentum region $10 < p_{T,jet} < 20 \text{ GeV}/c$. That means that the axis of the jet equals to the axis of the track. Therefore, the $\Delta R = 0$ gives us a point at the first bin.

Figure 6.6 shows the momentum dispersion distributions with the resolution parameter $R = 0.2$. The simulation results are performed in two intervals of jet transverse momentum: $10 < p_{T,jet} < 20$ and $20 < p_{T,jet} < 30$.

Figure 6.7 shows the momentum dispersion distributions with the resolution

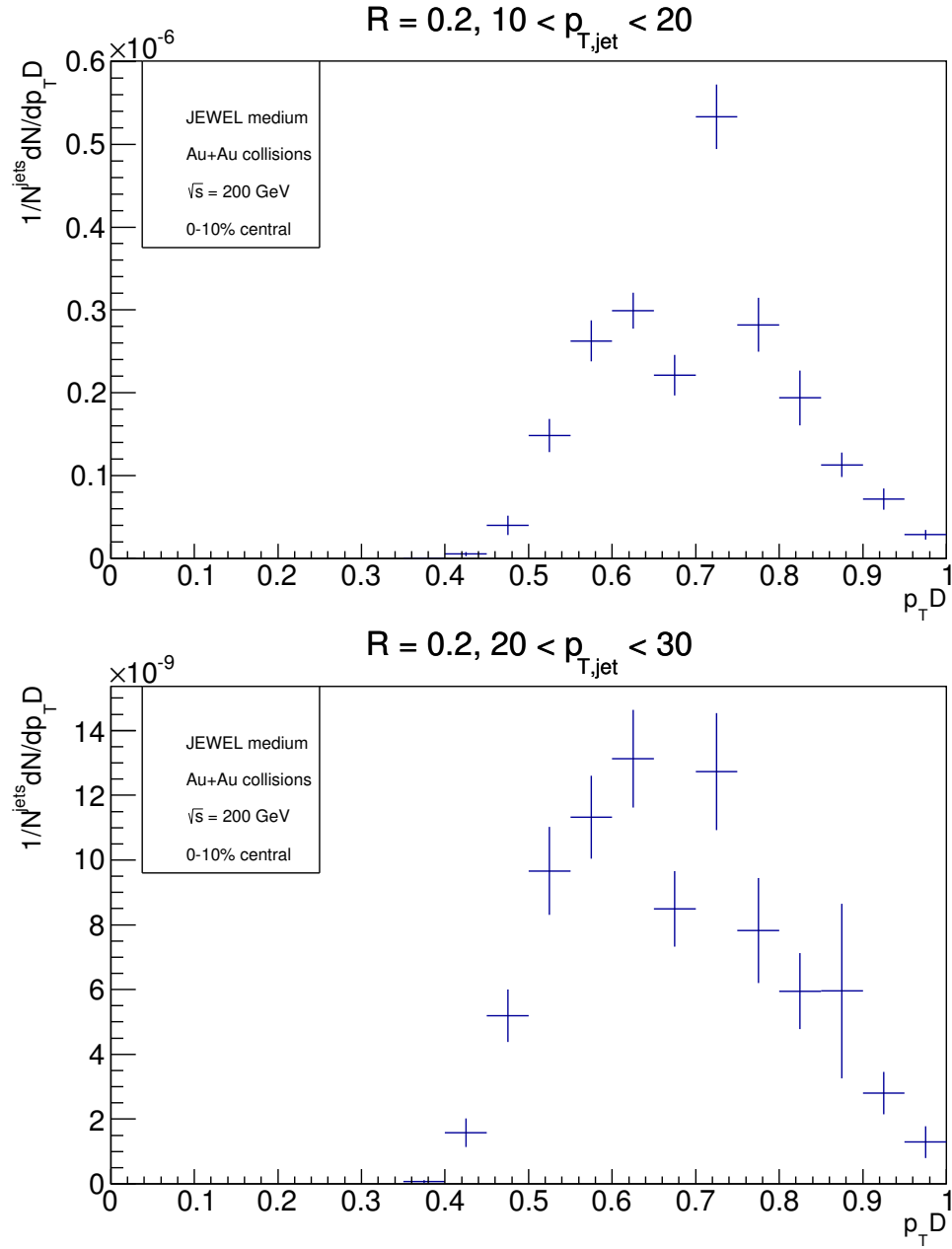


Figure 6.6: The momentum dispersion distributions of data simulated with the resolution parameter $R = 0.2$ for two $p_{T,\text{jet}} \in < 10; 20 >$ GeV/c (upper one) and $p_{T,\text{jet}} \in < 20; 30 >$ GeV/c (lower one).

parameter $R = 0.4$. The simulation results are performed in two intervals of jet transverse momentum: $10 < p_{T,\text{jet}} < 20$ and $20 < p_{T,\text{jet}} < 30$.

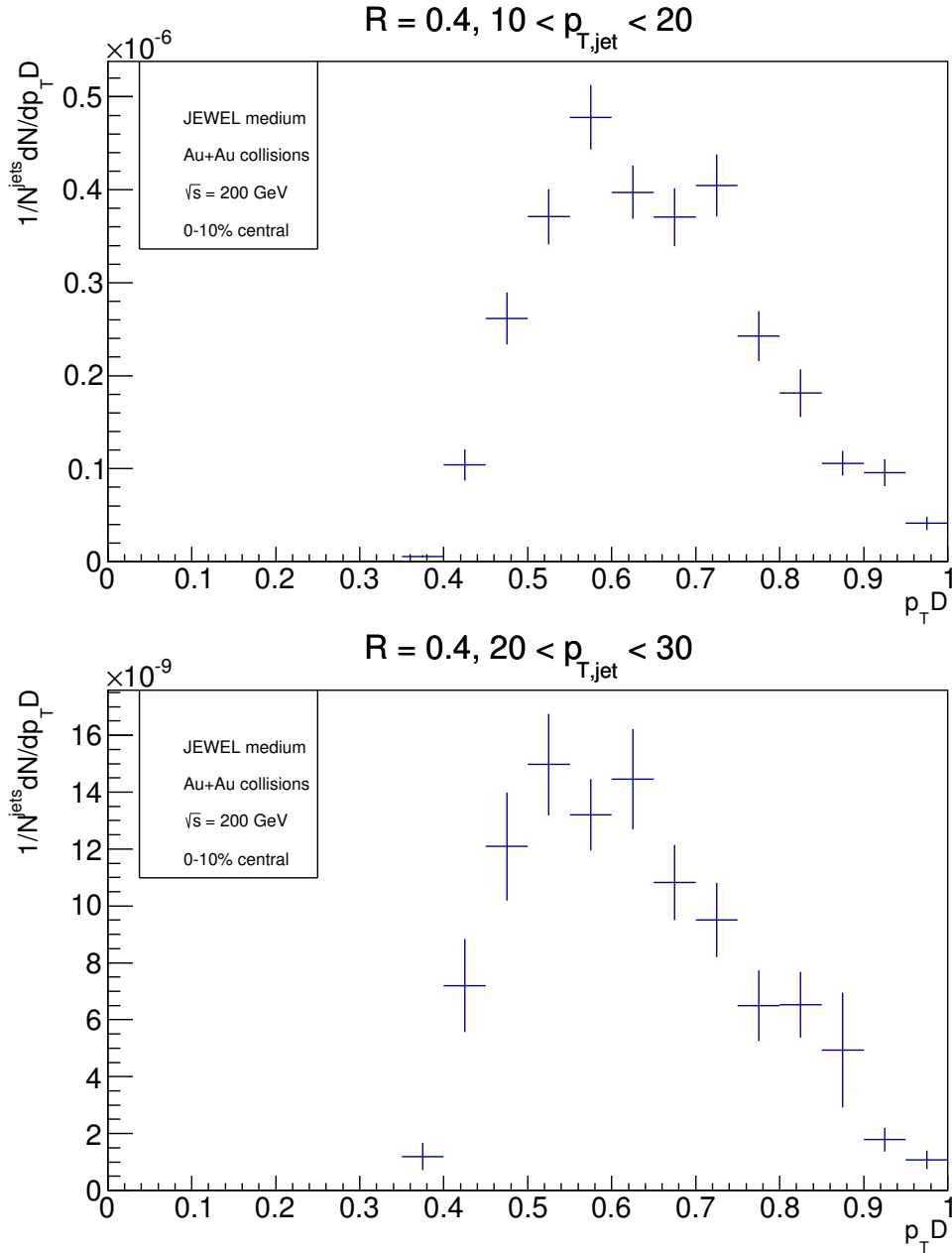


Figure 6.7: The momentum dispersion distributions of data simulated with the resolution parameter $R = 0.4$ for two p_T intervals: $p_{T,jet} \in < 10; 20 > \text{GeV}/c$ (upper plot) and $p_{T,jet} \in < 20; 30 > \text{GeV}/c$ (lower plot).

6.2.2 Results for the simulation without medium

The p_T spectra of charged jets with the resolution parameters $R = 0.2$ and $R = 0.4$ are depicted in Figure 6.8. Both spectra have the exponential shape. At the high- p_T region the spectra tend to 0.

Figure 6.9 shows the radial moment distributions of data simulated without medium with the resolution parameter $R = 0.2$. The simulation results are per-

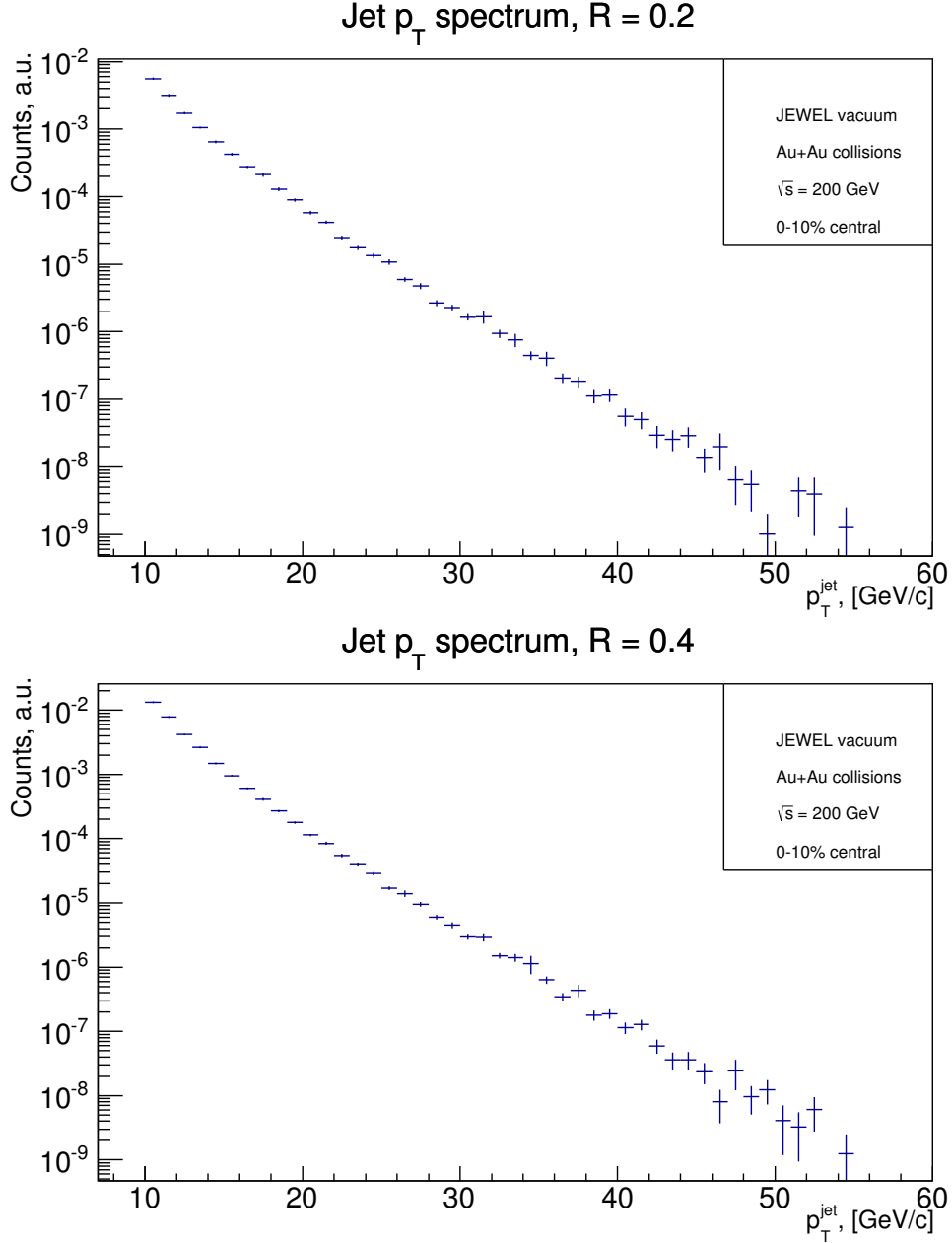


Figure 6.8: The p_T spectrum of charged jets for resolution parameter $R = 0.2$ (upper one) and $R = 0.4$ (lower one) of data simulated without medium.

formed in two intervals of jet transverse momentum: $10 < p_{T,jet} < 20$ (upper plot) and $20 < p_{T,jet} < 30$ (lower plot).

Figure 6.10 shows the radial moment distributions of data simulated without medium with the resolution parameter $R = 0.4$. The simulation results are performed in two intervals of jet transverse momentum: $10 < p_{T,jet} < 20$ (upper one) and $20 < p_{T,jet} < 30$ (lower one).

As in previous Subsection 6.2.1 it can be seen from the Figure 6.9 and Figure 6.10, there are points for $g < 0.01$, which are located higher for the transverse

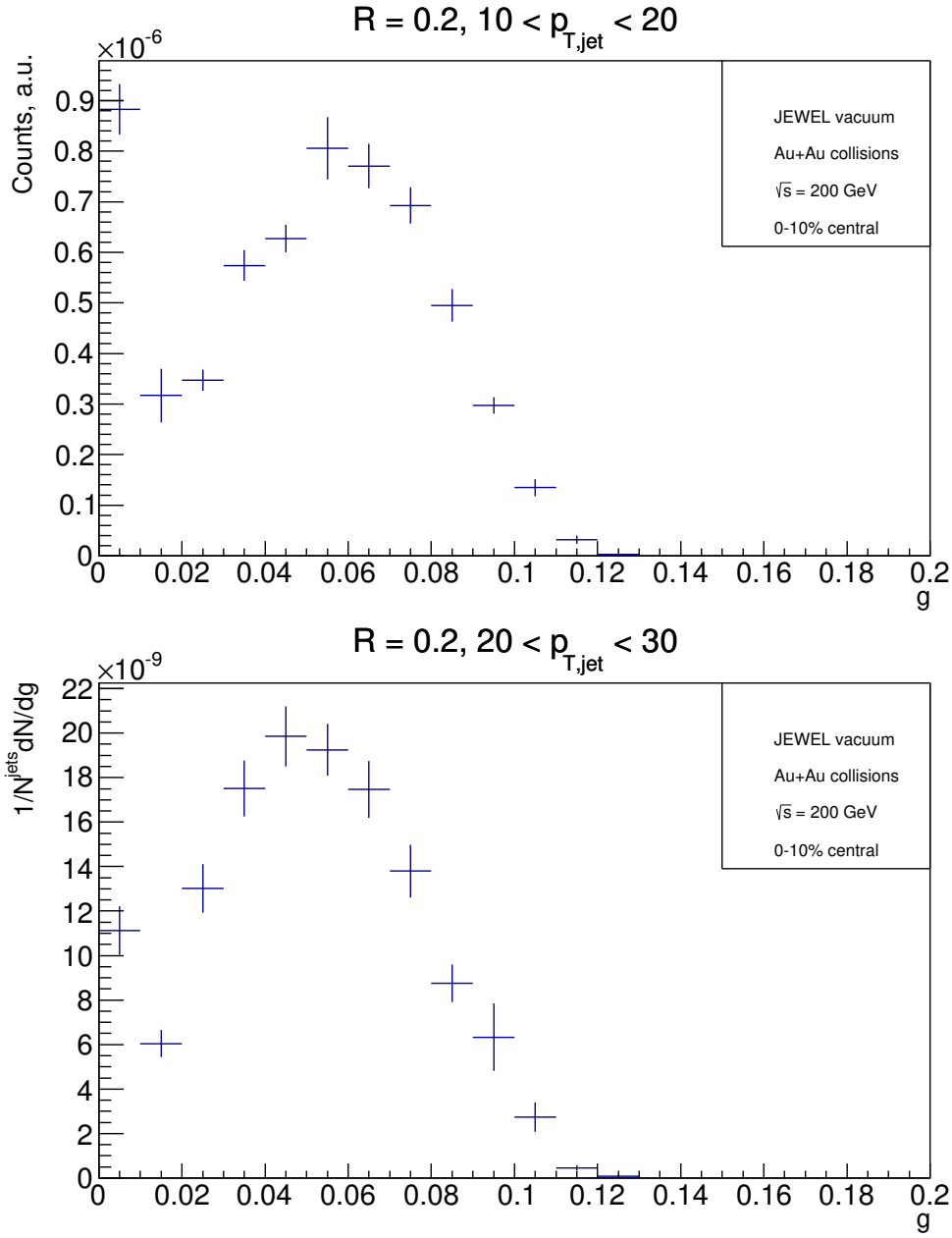


Figure 6.9: The radial moment distributions of data simulated with the resolution parameter $R = 0.2$ for two $p_{T,jet}$ intervals: $p_{T,jet} \in [10; 20]$ GeV/c (upper one) and $p_{T,jet} \in [20; 30]$ GeV/c (lower one).

momentum region $10 < p_{T,jet} < 20$ GeV/c. The reason for these points is the same. In comparison to the graphs of radial moment distributions for the simulation with medium we get higher peaks for the radial moment distributions for the simulation without medium for both resolution parameters and $p_{T,jet}$ regions.

Figure 6.11 shows the momentum dispersion distributions with the resolution parameter $R = 0.2$. The simulation results are performed in two intervals of jet transverse momentum: $10 < p_{T,jet} < 20$ and $20 < p_{T,jet} < 30$.

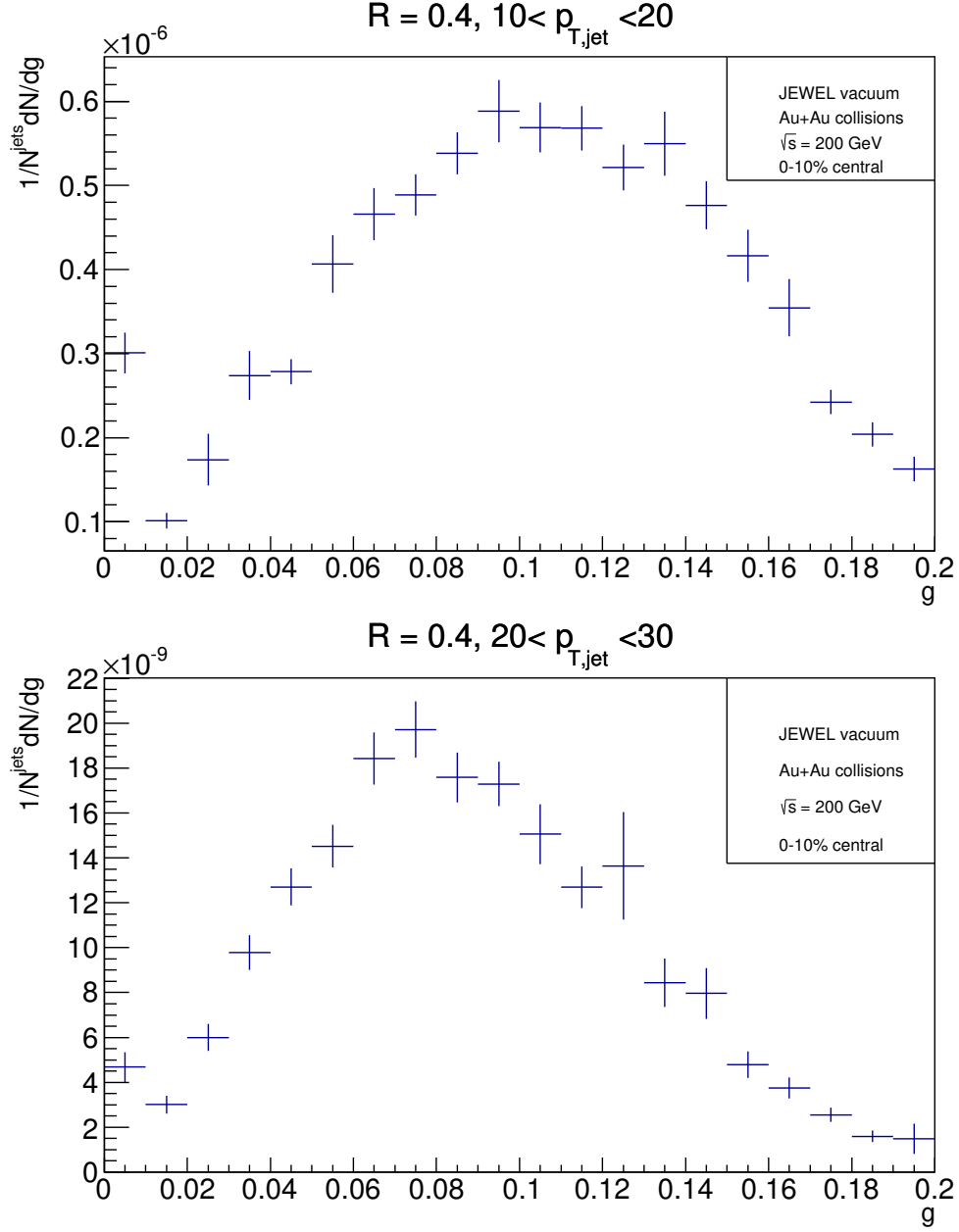


Figure 6.10: The radial moment distributions of data simulated with the resolution parameter $R = 0.4$ for two p_T intervals: $p_{T,jet} \in < 10; 20 > \text{GeV}/c$ (upper plot) and $p_{T,jet} \in < 20; 30 > \text{GeV}/c$ (lower plot).

Figure 6.12 shows the momentum dispersion distributions with the resolution parameter $R = 0.4$. The simulation results are performed in two intervals of jet transverse momentum: $10 < p_{T,jet} < 20$ and $20 < p_{T,jet} < 30$.

As for the radial moment distributions, we get higher peaks in momentum dispersion distributions for the simulation without medium.

All the figures depicted above have the same range for the radial moment and momentum dispersion as in Figure 6.1. However, the height of our distributions

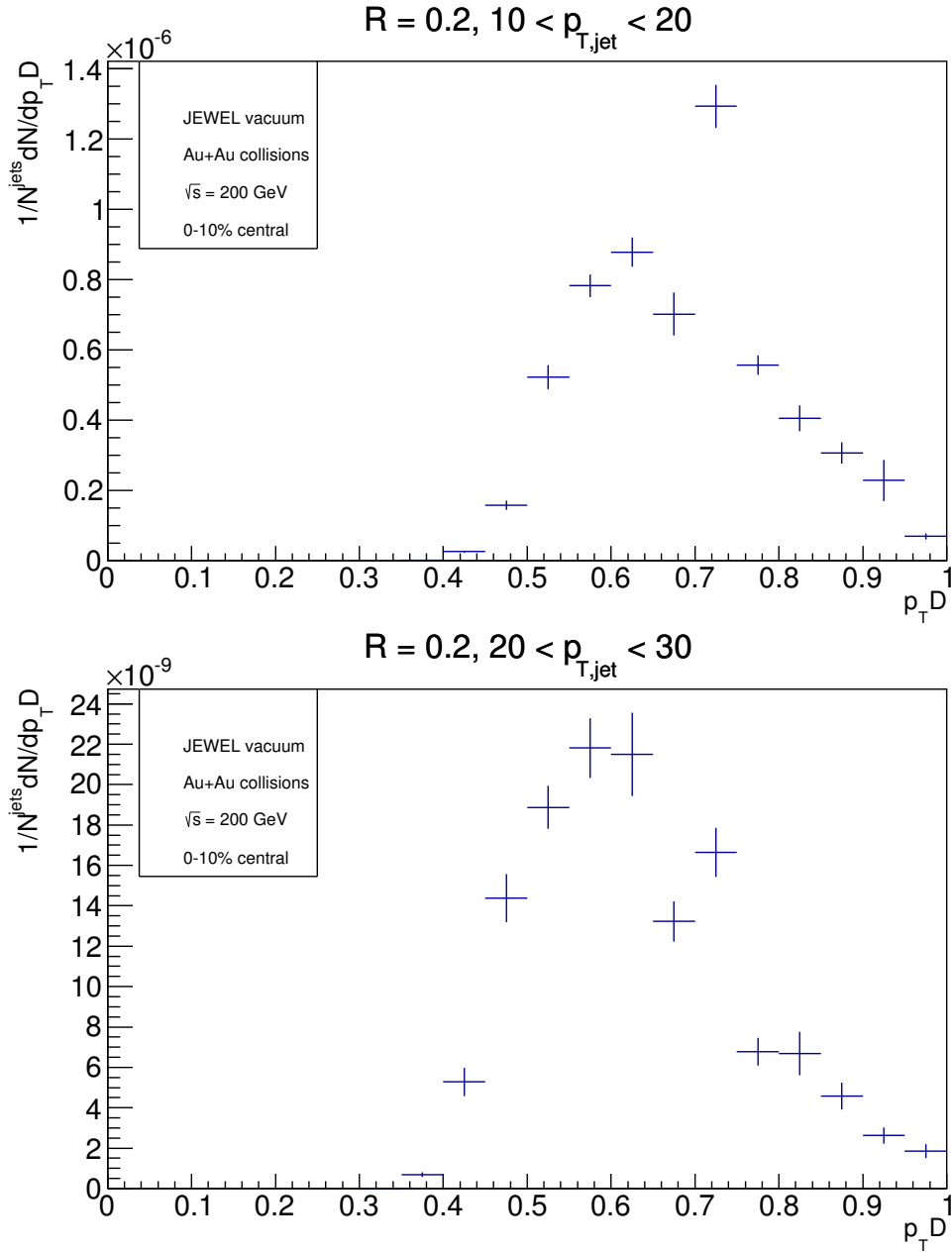


Figure 6.11: The momentum dispersion distributions of data simulated with the resolution parameter $R = 0.2$ for two $p_{T,jet}$ intervals: $p_{T,jet} \in [10; 20)$ GeV/c (upper one) and $p_{T,jet} \in [20; 30)$ GeV/c (lower one).

is significantly smaller than the height of the peaks on graphs of ALICE data. Such big difference could be due to the fact, that we had lower p_T regions.

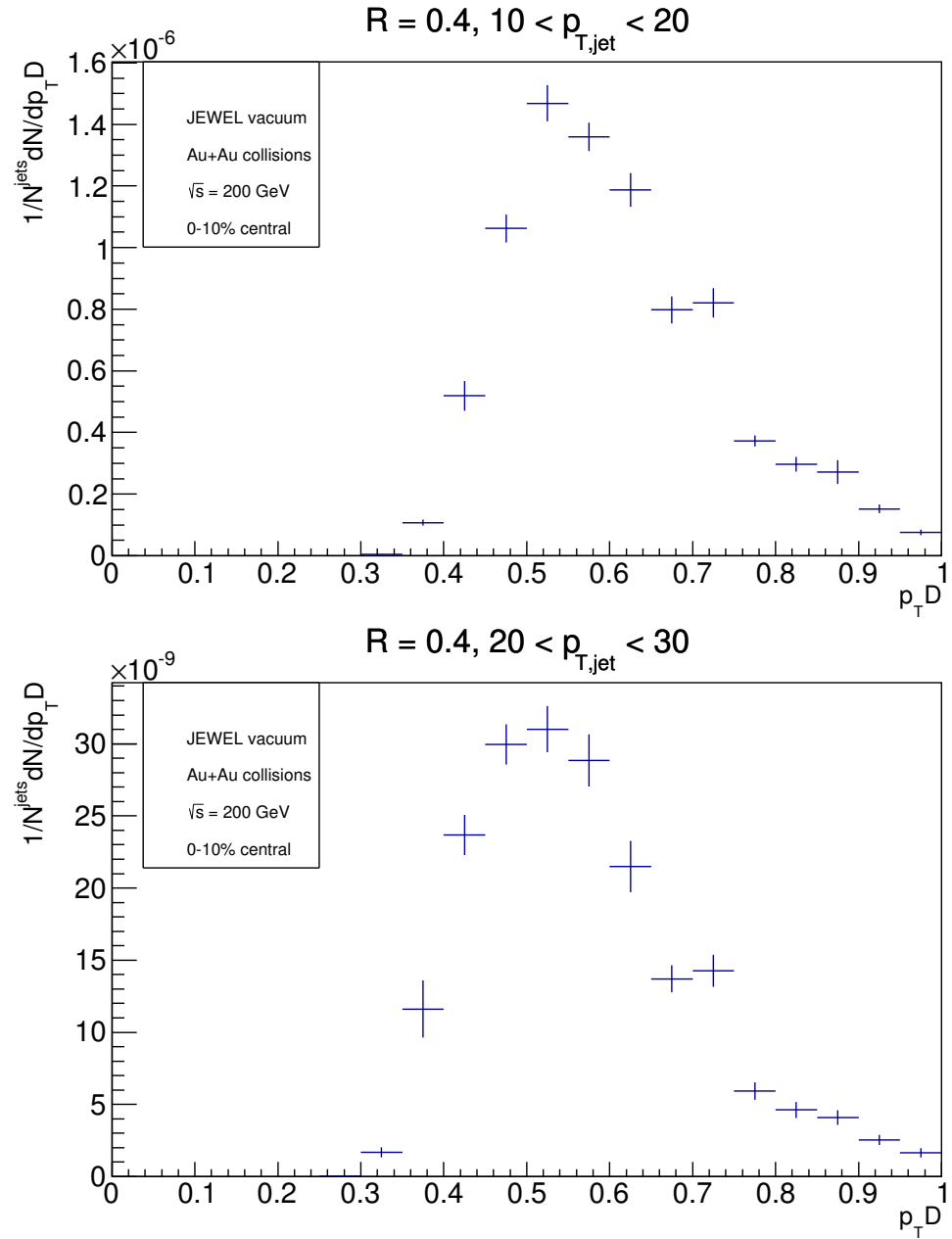


Figure 6.12: The momentum dispersion distributions of data simulated with the resolution parameter $R = 0.4$ for two $p_{T,jet} \in < 10; 20 >$ GeV/c (upper plot) and $p_{T,jet} \in < 20; 30 >$ GeV/c (lower plot).

Chapter 7

Summary

The nuclear-nuclear collisions at energies attainable at accelerators RHIC at BNL or the LHC at CERN are an ideal environment for studying the quark-gluon plasma, the hot and dense nuclear matter consisting of free partons. One of the most important probes of the nuclear matter is study of jet production. The QGP can be found in the early Universe or at the center of compact stars, but in this thesis we focused on the QGP that is produced in the initial stages of heavy-ion collisions at RHIC, mainly at the STAR experiment.

In the first chapter a brief introduction to particle physics was presented focusing on the description of fundamental interactions and the Standard Model. The second chapter was dedicated to the physics of nucleus-nucleus collisions. In that chapter the two observables needed to measure elusive characteristics of the QGP were described. The first one, the anisotropic flow, is a very important probe of the earliest stages of the collision. The momentum anisotropy of produced particles is quantified by the Fourier expansion of the measured momentum distribution of particles, where the second coefficient v_2 is called the elliptic flow. The second observable was the nuclear modification factor R_{AA} , which is a measure of modification of particle production or jet production in nuclear medium relative to elementary proton-proton collisions. The third chapter described the most important parts of the STAR detector system used for studying jets. These are the Time Projection Chamber, the Time Of Flight system, the Barrel-Electromagnetic Calorimeter and the Heavy Flavor Tracker.

The main aim of this Bachelor's thesis was to acquaint with the modern jet reconstruction algorithms and basic jet shape observables. Within the framework of this thesis the cluster-type jet finding algorithms were mainly described because of their effectiveness and infrared and collinear safety in comparison to cone jet finding algorithms. The kT algorithm is not suitable for jet studies due to its sensitivity to large background and is mostly used for the background estimation. The anti-kT algorithm is not so sensitive to the large background in heavy-ion collisions and therefore is commonly used in heavy-ion collisions to study jet properties. Both these jet finding algorithms and many others are implemented in the FastJet software package which was used in the practical part of this thesis.

The practical part of this thesis focused on the application of the anti-kT jet finding algorithm applied on the data simulated by the Monte-Carlo generator JEWEL, which is described in the fifth chapter. From the large variety of jet shape observables which were studied in the fifth chapter, the radial moment and momentum

dispersion were chosen. The obtained results of the JEWEL simulation are briefly summarized in the last chapter together with their comparison to available results from the ALICE experiment at the LHC.

This Bachelor's thesis serves as my preparation for further analysis of jets measured in Au+Au collisions at $\sqrt{s_{NN}} = 200$ GeV at the STAR experiment at RHIC.

Bibliography

- [1] The Standard Model. The picture taken from: https://en.wikipedia.org/wiki/Standard_Model#/media/File:Standard_Model_of_Elementary_Particles.svg. [online 10.5.2017].
- [2] S. Bushwick. How Low Can RHIC Go? https://www.bnl.gov/today/body_pics/2010/07/phases-of-QCD-350px.jpg. [online 15.4.2017].
- [3] R. Stock. Relativistic Nucleus-Nucleus Collisions and the QCD Matter Phase Diagram. [arXiv 0807.1610]. 2008.
- [4] T. Schuster M. Kliemant, R. Sahoo and R. Stock. Global properties of nucleus-nucleus collisions. In The Physics of the Quark-Gluon Plasma. http://www.beck-shop.de/fachbuch/leseprobe/9783642022852_Excerpt_001.pdf.
- [5] K. Yagi, T. Hatsuda, Y. Miake. Quark-Gluon Plasma. Cambridge University Press, 2005.
- [6] The picture is taken from: <http://www.quantumdiaries.org/wp-content/uploads/2011/02/FlowPr.jpg>. [online 13.5.2017].
- [7] J. Adams et. al STAR. Particle type dependence of azimuthal anisotropy and nuclear modification of particle production in Au + Au collisions at $\sqrt{s_{NN}} = 200$ GeV. *Phys. Rev. Lett.* 92:052302, 2004.
- [8] A. Adare et. al. PHENIX. Neutral pion production with respect to centrality and reaction plane in Au+Au collisions at $\sqrt{s_{NN}} = 200$ GeV, [arXiv: 1208.2254], 2013.
- [9] L. Adamczyk et. al STAR. Measurements of jet quenching with semi-inclusive hadron+jet distributions in Au+Au collisions at $\sqrt{s_{NN}} = 200$ GeV, [arXiv 1702.01108]. 2017.
- [10] J. Rusňák. Charged jet reconstruction in Au+Au collisions at $\sqrt{s_{NN}} = 200$ GeV at RHIC. [arXiv:1412.2111], 2015.
- [11] Brookhaven National Laboratory. RHIC. <https://www.bnl.gov/rhic/>. [online 5.5.2017].
- [12] Brookhaven National Laboratory. The STAR experiment. <https://www.star.bnl.gov/>. [online 5.5.2017].

-
- [13] M. Anderson, J. Berkovitz, W. Betts et.al. The STAR Time Projection Chamber: A Unique Tool for Studying High Multiplicity Events at RHIC. 2003.
- [14] M. R. Lomnitz. Ph.D. thesis. Measurement of charmed meson azimuthal anisotropy in Au+Au collisions at $\sqrt{s_{NN}} = 200$ GeV at RHIC (189 pp.). https://drupal.star.bnl.gov/STAR/files/Dissertation_submit.pdf.
- [15] The STAR TOF collaboration. Proposal for a large area Time Of Flight system for STAR. https://www.star.bnl.gov/public/tof/publications/TOF_20040524.pdf, 2004.
- [16] M. Beddo, E. Bielick, T. Fornek et.al. The STAR Barrel Electromagnetic Calorimeter. https://www.star.bnl.gov/public/tpc/NimPapers/emc/emc_nim.pdf, 2002.
- [17] BNL RHIC. Heavy Flavor Tracker for STAR. <https://www.bnl.gov/rhic/news2/news.asp?a=4657&t=today>. [online 6.5.2017].
- [18] F. Tanedo. The picture is taken from: <http://www.quantumdiaries.org/wp-content/uploads/2011/04/clustering.png>. [online 1.12.2016].
- [19] G. C. Blazey et. al. Run II jet physics, [hep-ex/0005012]. pages 47–77, 2000.
- [20] G. Soyez M. Cacciari, G. P. Salam. The Anti-k(t) jet clustering algorithm. *JHEP*, 04:063, 2008.
- [21] M. Cacciari, G. P. Salam. Dispelling the N^3 myth for the k_t jet-finder. *Phys. Lett.*, B641:57-61, 2006.
- [22] K. C. Zapp. JEWEL 2.0.0: Directions for use. *Eur. Phys. J.*, C74(2):2762, 2014.
- [23] K. C. Zapp. Geometrical aspects of jet quenching in JEWEL, *Phys. Lett.*, B735:157–163, 2014.
- [24] D. Caffarri. Exploring jet substructure with jet shapes in ALICE, [arXiv: 1704.05230]. 2017.
- [25] S. Acharya et. al ALICE. First measurement of jet mass in Pb–Pb and p–Pb collisions at the LHC. [arXiv: 1702.00804]. 2017.
- [26] V. Petráček. Subatomová fyzika I. 2009.
- [27] A. Adare et al. Suppression pattern of neutral pions at high transverse momentum in Au + Au collisions at $\sqrt{s_{NN}} = 200$ GeV and constraints on medium transport coefficients, *Phys. Rev. Lett.*, 101 232301, 2008.
- [28] C. Chasman, D. Beavis, R. Debbe et.al. A Heavy Flavor Tracker for STAR. http://rnc.lbl.gov/~wieman/hft_final_submission_version.pdf. [online 6.5.2017].
- [29] M. Cacciari, G. P. Salam, G. Soyez. FastJet user manual. [arXiv: 1111.6097]. 2012.

BIBLIOGRAPHY

- [30] M. Cacciari, G. P. Salam, G. Soyez. The Catchment Area of Jets, *JHEP*, 04:005, 2008.
- [31] M. Cacciari, G. P. Salam. Pileup subtraction using jet areas. *Phys. Lett.*, B659:119-126, 2008.
- [32] R. Placakyte. Parton Distribution Functions. [arXiv: 1111.5452], 2011.
- [33] L. Cunqueiro. Jet shapes in pp and Pb–Pb collisions at ALICE. *Nucl. Phys.*, A956:593–596, 2016.